Master's thesis

NTNU
Norwegian University of Science and Technology
Faculty of Natural Sciences
Department of Materials Science and Engineering

Amalie Strømme Falck

Pulsed laser growth of La_2NiMnO_6 for intermediate band solar cells

Master's thesis in Nanotechnology
Supervisor: Ingrid Hallsteinsen
June 2022

NTNU
Norwegian University of
Science and Technology

Amalie Strømme Falck

Pulsed laser growth of La_2NiMnO_6 for intermediate band solar cells

Master's thesis in Nanotechnology
Supervisor: Ingrid Hallsteinsen
June 2022

Norwegian University of Science and Technology
Faculty of Natural Sciences
Department of Materials Science and Engineering

NTNU
Norwegian University of
Science and Technology

Abstract

Intermediate band solar cells show great potential to increase the efficiency of photovoltaics, while reducing the cost of the generated electricity. Functional oxide double perovskites are among the candidate materials for intermediate band solar cells, as additional energy states can be introduced in the band structure through periodic ordering of the cations. In these materials, the functional properties are closely related to the atomic structure. Thus, control of the ordering of atoms in the material is a prerequisite for manipulation of the functional properties.

In this work, thin films of La_2NiMnO_6 (LNMO) were grown on (111)-oriented $SrTiO_3$ substrates by pulsed laser deposition. Substrate surface preparation by DI-water etching and high-temperature annealing was optimized to yield a uniform step-and-terrace surface structure, providing a green alternative to the standard procedure of etching with hydrofluoric acid. LNMO films were successfully grown with a morphology that duplicated the substrate surface, hence control of the film surface structure was obtained. The target-substrate distance during deposition was found to have minimal impact on the growth mode of the initial layers, whereas the surface roughness was found to increase with film thickness. A gradual transition from layer-by-layer growth to island growth was observed by atomic force microscopy and reflection high-energy electron diffraction. The critical thickness for growth relaxation was delayed by growth on step-bunched substrates. Further, x-ray diffraction and electron microscopy studies confirm that the films are crystalline. Magnetic measurements from vibrating-sample magnetometry show no indications of ferromagnetic phases, suggesting that the grown films are non-stoichiometric.

Thin films of LNMO were grown with control of the surface structure, although controlled ordering of cations was not confirmed. For further development, it is suggested that the oxygen pressure or the substrate temperature is increased during deposition, to improve stoichiometry and promote growth of films with functional properties.

Sammendrag

Mellombåndssolceller har vist stort potensiale for å øke effektiviteten til fotoelektriske enheter, og samtidig redusere kostnaden knyttet til produsert elektrisitet. Funksjonelle oksidmaterialer, som doble perovskitter, er kandidater for benyttelse som absorbsjonslag i mellombåndssolceller, fordi ekstra energitilstander kan introduseres i båndstrukturen når kationene i materialet ordnes periodisk. I disse materialene er de funksjonelle egenskapene tett knyttet til den atomære strukturen. Derfor er kontroll på ordningen av atomene en forutsetning for å kunne styre og manipulere de funksjonelle egenskapene.

I dette arbeidet ble tynnfilmer av La_2NiMnO_6 (LNMO) grodd på substrat av (111)-orientert $SrTiO_3$ ved bruk av pulsert laserdeponering. Substratpreparering ble gjennomført ved bruk av DI-vann og høytemperaturgløding, og prosessen ble optimalisert for å gi en periodisk trinn- og terrassestruktur. Metoden er et trygt og miljøvennlig alternativ til dagens standard prosedyre, som baserer seg på etsning av overflaten med flussyre. Overflaten til de grodde tynnfilmene speilet strukturen til substratet de ble grodd på, og kontroll på filmens morfologi ble derfor oppnådd. Avstanden mellom kildemateriale og substrat under deponering hadde liten påvirkning på vekstmoden for de første lagene av filmen, mens det ble observert at overflateruheten til filmene økte med filmtykkelse. En gradvis overgang fra lagvis- til tredimensjonal vekst ble observert ved bruk av atomær kraftmikroskopi og refleksjons høyenergi elektrondiffraksjon. Den kritiske tykkelsen, der veksten slutter å være epitaksiell og det går over til tredimensjonal vekst, er vist å øke på substrat med sammenvokste terrasser. Videre bekrefter karakterisering ved røntgendiffraksjon og transmisjonselektronmikroskopi at de grodde filmene er krystalline. Magnetiske målinger fra vibrerende-prøve magnetometri viser ingen tegn til ferromagnetiske faser, noe som indikerer at de grodde filmene ikke er støkiometriske.

Tynnfilmer av LNMO ble grodd med god kontroll på overflatestrukturen, skjønt ordning av kationer ikke har blitt bekreftet. For videre utvikling av vekstprosessen foreslås det å øke oksygentrykket eller substrattemperaturen under deponering for å forbedre støkiometri, og dermed fremme vekst av filmer med funksjonelle egenskaper.

Preface and Acknowledgements

This master thesis is written and submitted as the final project of the Master of Science degree in Nanotechnology at the Norwegian University of Science and Technology. As this is not a continuation of a specialization project, all experimental work was performed during the spring semester of 2022, at laboratory facilities at the Department of Material Science, Department of Electronic Systems, Department of Mechanical and Industrial Engineering, and NTNU Nanolab. In addition, TEM studies were performed by Iryna Zelenina at the Department of Physics. All figures in this thesis are made by the author, unless otherwise specified.

I would like thank to my supervisor, Associate Professor Ingrid Hallsteinsen, for her guidance, support and invaluable feedback throughout the work of this project. Her expertise within functional oxides and genuine excitement for nanoscience has been extremely helpful and inspirational. Thanks also to the rest of the PLD-group, Johannes, Yu and Damian, for always being available to answer my questions and help out in the PLD lab. Likewise, I would like to thank Jakob at Nanolab for extensive help with the AFM. I am grateful for the help I have received with characterization of the thin films that were grown during the project, especially from Jonas Lyng-Jørgensen, Yu Liu, Stephanie Birgit Burgmann, Iryna Zelenina, Viviann Hole and Tron-Arne Nilsen. The Research Council of Norway is acknowledged for the Norwegian Micro- and Nano-Fabrication Facility, NorFab, project number 295864.

Finally, I would like to express gratitude to my family and friends for their unconditional love and support. Especially thanks to my fellow students in Timini, whom made the years as a student i Trondheim so amazing.

Amalie Strømme Falck
Trondheim, June 20th, 2022

Contents

Abstract i

Sammendrag i

Preface ii

Abbreviations vi

1 Introduction 1
- 1.1 Aim of work . . . 2
- 1.2 Outline . . . 2

2 Theory 4
- 2.1 Intermediate band solar cells . . . 4
  - 2.1.1 Solar cells based on complex oxides . . . 5
- 2.2 Material system . . . 6
  - 2.2.1 An introduction to perovskites . . . 6
  - 2.2.2 Double perovskites . . . 7
- 2.3 Preparation of STO(111) substrates . . . 9
  - 2.3.1 Motivation to use STO(111) . . . 9
  - 2.3.2 State of the art . . . 11
- 2.4 Thin film growth . . . 12
  - 2.4.1 Growth modes . . . 12
  - 2.4.2 Film growth by pulsed laser deposition . . . 14
  - 2.4.3 Monitoring the growth process by RHEED . . . 16
- 2.5 State of the art PLD growth of double perovskites . . . 18
  - 2.5.1 Ferromagnetism in LNMO . . . 18

3 Experimental procedures 21
- 3.1 Substrate preparation . . . 21
- 3.2 Film growth . . . 22
- 3.3 Characterization . . . 23
  - 3.3.1 Atomic force microscopy . . . 23
  - 3.3.2 Lateral force microscopy . . . 24
  - 3.3.3 X-ray diffraction . . . 24

3.3.4 Raman spectroscopy . . . 25
3.3.5 Transmission electron microscopy . . . 25
3.3.6 Ellipsometry . . . 25
3.3.7 Vibrating-sample magnetometry . . . 25

4 Results **27**
4.1 Substrate preparation of (111)-oriented STO . . . 27
4.1.1 Effect of water purity . . . 28
4.1.2 Effect of annealing temperature and dwell time . . . 29
4.1.3 Lateral force microscopy . . . 31
4.2 Effect of target-substrate distance on initial film growth . . . 32
4.3 Evolution of the growth mode throughout the growth process . . . 34
4.4 RHEED characterization of film growth . . . 37
4.4.1 Diffraction pattern from substrate . . . 37
4.4.2 Diffraction pattern during deposition . . . 38
4.4.3 Sensitivity of the specular spot intensity to external factors . . . 38
4.4.4 Specular spot intensity tracking during deposition . . . 40
4.5 X-ray diffraction . . . 42
4.6 Raman spectroscopy . . . 43
4.7 Transmission electron microscopy . . . 45
4.8 Ellipsometry . . . 45
4.9 Vibrating-sample magnetometry . . . 46

5 Discussion **47**
5.1 Substrate preparation . . . 47
5.1.1 Water purity during etching . . . 47
5.1.2 Annealing parameters . . . 48
5.2 Film growth . . . 50
5.2.1 Effect of substrate surface morphology on film growth . . . 50
5.2.2 Effect of target-substrate distance on the initial growth mode . . . 50
5.2.3 Growth evolution evaluated by AFM . . . 52
5.2.4 Growth mode evaluated by RHEED . . . 53
5.2.5 Measurements of film thickness . . . 55
5.2.6 Effect of glue on substrate temperature and growth mode . . . 56
5.2.7 Summary of key findings . . . 57
5.3 Measurements of crystallinity . . . 57
5.3.1 TEM . . . 57
5.3.2 XRD . . . 58
5.3.3 Raman spectroscopy . . . 59
5.4 Magnetic properties . . . 59
5.5 Optical properties . . . 60

6 Further Work **62**

7 Conclusion **64**

Bibliography **65**

A Parameters during pulsed laser deposition **71**

B Additional XRD measurements **73**

Abbreviations

AFM Atomic Force Microscopy

BHF Buffered Hydrofluoric Acid

DI-water De-ionized water

HF Hydrofluoric Acid

IB Intermediate Band

IBSC Intermediate Band Solar Cell

LAO $LaAlO_3$

LFM Lateral Force Microscopy

LNMO La_2NiMnO_6

LSAT $(La_{0.3}SrO_7)(Al_0.65Ta_0.35)O_3$

MSE Mean Squared Error

PLD Pulsed Laser Deposition

RHEED Reflection High Energy Electron Diffraction

STEM Scanning Transmission Electron Microscopy

STO $SrTiO_3$

TEM Transmission Electron Microscopy

UP-water Ultra-pure water

VSM Vibrating-Sample Magnetometry

XRD X-ray Diffraction

XRR X-ray Reflectivity

Chapter 1

Introduction

The energy demand of the world is continuously increasing, while global warming demonstrates the need to replace carbon-based methods of energy production [1]. Among the renewable energy sources, sunlight is of uttermost importance due to its abundance. Although single junction Si-based solar cells are increasing in numbers, their efficiency is limited to 33.16% by the Shockley-Queisser limit [2]. In the search for supplementary, high power conversion efficiency materials, perovskites prove to be a strong candidate due to their multiferroic properties, suitable bandgaps and low production costs. As solar absorbers, they can provide long carrier diffusion lengths, low recombination losses, low cost, and bandgap tunability [3, 4]. Despite the extensive development over the last decade, the highest performing organic-inorganic perovskite cells demonstrated to date possess challenges of instability and moisture sensitivity that cause degradation. Additionally, many materials contain toxic lead [5]. These drawbacks drive research on development and optimization of new candidate materials.

La_2NiMnO_6 (LNMO), a complex oxide with the perovskite structure, where the B-site cations consist of 50% Ni and 50% Mn, is one such material that has demonstrated a power conversion efficiency of 15.42% [3, 6, 7]. Additional electronic band states can be introduced between the valence band and conduction band, to allow for increased utilization of the solar spectra through absorption of lower-energy photons. By ordering of the B-site cations or Bi-doping [8], intermediate band states can be introduced in double perovskites and substantially increase the efficiency, up to 62% for one intermediate band and 72% for two intermediate bands [8], by absorbing more of the solar spectrum.

Exploiting these possibilities requires precise control of the atomic structure, which can be achieved by fabrication through pulsed laser deposition. For the development of such materials, an increased understanding of the influence of crystal parameters, like the B-site ordering and doping, is needed. However, advanced insights in the growth modes of thin films during pulsed laser deposition is first required to control the epitaxy, crystal structure, and cation ordering in the deposited film, and subsequently open the door for full exploitation of the functional properties.

1.1 Aim of work

This master thesis is part of a larger research project on oxide-based intermediate band materials, which goal is to understand how novel sustainable materials for solar cells can be designed using advanced physical deposition techniques. These techniques allow us to control and engineer small changes in the atomic structure, resulting in new functional properties. A prerequisite for such precise engineering is a high degree of control of the material surfaces and the deposition process. In particular, the PLD technique has a large parameter space, where variations in all deposition parameters can influence the growth mode, crystal quality and stoichiometry, and thereby the properties, of the final material. This master thesis aims to increase the understanding of pulsed laser growth of LNMO thin films on (111)-oriented STO substrates, where the first goal is to grow high-quality films.

The first objective of this thesis is to develop a procedure for preparation of substrates with a periodic, reproducible, and well-defined step-and-terrace structure. Such a surface is typically achieved through etching with hydrofluoric acid, while this work aims to achieve the same degree of structural and chemical ordering by etching with de-ionized water, thereby avoiding the use of a toxic and hazardous acid with associated risk for both people and the environment [9]. Different substrate preparation procedures are investigated in terms of water purity, annealing time, and temperature. The resulting surface topography is characterized by atomic force microscopy (AFM).

The next objective is to optimize and characterize the growth of thin films. Herein, two variables of interest are considered. The effect of target-substrate distance on the growth mode of the initial monolayers of the film is studied, as previous work in the lab has indicated a possible dependency [10]. Next, relaxation of the growth mode from layer-by-layer to island growth is identified by comparison of the surface roughness of films grown by 500, 1500, 2000 and 4000 pulses. For characterization, AFM and reflection high-energy electron diffraction (RHEED) is used. X-ray diffraction (XRD), transmission electron microscopy (TEM), and Raman spectroscopy studies are performed to assess the epitaxy and crystal structure of selected films.

The final objective is to characterize the functional properties of the deposited films, as it can confirm if the utilized growth process produces films that are stoichiometric and with high crystal quality, as is important for the utilization of LNMO as a light-absorbing material. Specifically, the magnetic properties are characterized by vibrating-sample magnetometry (VSM) and the optical constants are characterized by ellipsometry.

1.2 Outline

This thesis is organized as follows. Chapter 2 covers theory on the material system, thin film growth modes and pulsed laser deposition, in addition to an introduction to state-of-

the-art preparation of (111)-oriented STO substrates and pulsed laser growth of double perovskite LNMO. In Chapter 3, the experimental methods for substrate preparation, thin film growth and thin film characterization are described. The results are presented in Chapter 4, along with a discussion of their significance in Chapter 5. Next, suggestions for further work are given in Chapter 6, before some concluding remarks are made in Chapter 7.

Chapter 2

Theory

This chapter will provide the theory related to this master thesis. First, an introduction to intermediate band solar cells is provided along with the motivation for use of double-perovskite LNMO for photovoltaic applications. Next, an introduction is given to the crystallographic properties of the material of interest, followed by a review of substrate preparation methods. Further, growth of thin films is presented, focusing on pulsed laser growth. Finally, the state-of-the-art growth of LNMO through PLD is covered.

2.1 Intermediate band solar cells

In intermediate band solar cells, additional band gaps are introduced to increase the overall efficiency of the material as a light absorber. This section largely follows [11], and covers the theoretical foundation of intermediate band solar cells (IBSC). In a photovoltaic materials, the energy of an incoming photon is transferred to an electron that is excited across the band gap, from the valence band to a higher-energy conduction band, producing free charge carriers. The energy from the photon can then be collected as current. A conventional single band gap solar cell can only collect energy from photons with energy equal to, or above, the band gap, and will simply extract the band gap energy for each excitation. When the solar spectrum is channeled into photo-converters with different band gaps, more of the solar spectrum can be harvested, and more energy is collected from each photo-induced excitation, thus allowing for higher power conversion efficiency. Intermediate band and multiple band cells support three or more such band gap transitions. This can be achieved in materials with more than two bands in the electronic band structure, for instance by an intermediate band state in the band gap as illustrated in Figure 2.1. Under illumination, electrons are excited from the valence band into both the conduction and intermediate band across E_G and E_H, and from the intermediate band to the conduction band across E_L. Suppose the intermediate and conduction bands are not thermally coupled, the electron population in the individual bands form local quasi-thermal equilibrium, with associated quasi-Fermi levels, E_F. The described intermediate

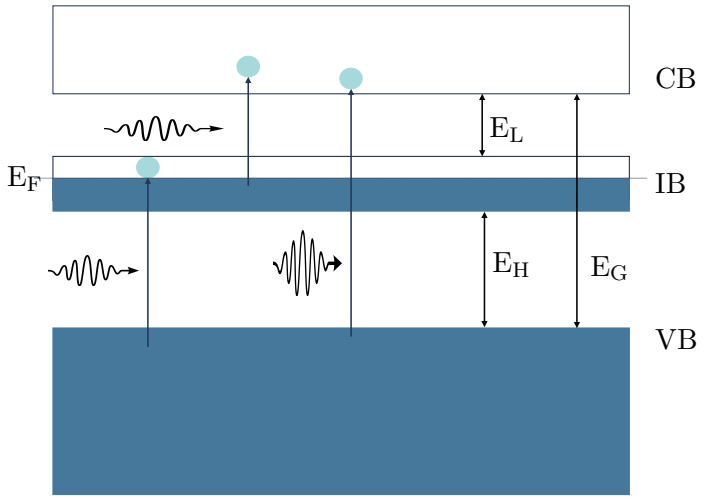

Figure 2.1: Energy band diagram of an IB solor cell with a single valence band (VB), and intermediate band (IB) and a conduction band (CB). The material has three band gaps: the VB to CB transition E_G, and the high- and low energy intermediate transitions, E_H and E_L.

band can be a result of the band structure, or it can be introduced via impurities or quantum heterostructures that introduce new electronic levels into the band gap [12].

2.1.1 Solar cells based on complex oxides

The performance of perovskite solar cells has increased tremendously since they were first introduced, now competing with the efficiency of commercial silicon solar cells [3, 4]. However, the cells with high efficiencies are based on hybrid organic-inorganic perovskites. Despite the outstanding photophysical properties, like long carrier diffusion length and high power-conversion efficiency, they have problems with instability due to moisture-induced corrosion and photo-oxidation. Additionally, lead content in these materials makes them toxic, limiting the possibility of global commercialization [5].

Inorganic oxide perovskites with substituted B-site cations, called double perovskites, have emerged as an interesting alternative for solar applications. In addition to large variety in structure and composition, they offer high material stability and appropriate band gaps that can be tuned through small changes in the crystal structure from doping or strain [3, 6, 13]. More specifically, band gaps between 1.0-1.6 eV can be achieved, with absorption as strong as the organic-inorganic hybrid counterpart $CH_3NH_3PbI_3$ [14]. Due to photoferroelectricity, the presence of both ferroelectric and photovoltaic properties in a material, the recombination rate is low compared to other intermediate-band systems. The depolarization field that is present due to the ferroelectric polarization, improves the separation of charge carriers and enhances the photovoltaic performance. Additionally, the field is helpful to extend the depletion region and increase built-in electric field, providing a significant improvement in the open-circuit voltage, V_{OC}, and short-circuit current, J_{sc}, of solar cells based on photoferroelectric perovskites [15].

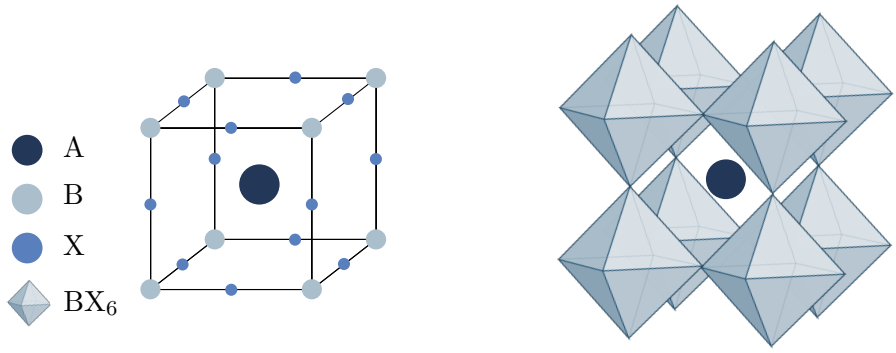

Figure 2.2: Schematic of the cubic perovskite a) unit cell showing all atoms and b) displaying the A-site cations and BX_6 octahedra.

Among the materials of interest is oxide double perovskite La_2NiMnO_6 (LNMO), that can have a direct band gap in the same region as silicon, $E_G = 1.1$ eV, with band gap energy between 1.1 eV and 1.4 eV [6, 7, 16]. In addition to a suitable narrow band gap, charge carrier life-time of ≈ 0.36 µs is reported [6]. In addition to the interest as traditional single band gap solar absorbers, it may be possible to introduce multiple band gaps in the oxide double perovskites like LNMO. These are introduced by cation ordering or doping with Bi^{5+}, that provide additional electronic band states, thus making the material broad-spectrum photo-absorbers [8, 17, 18].

2.2 Material system

2.2.1 An introduction to perovskites

Perovskites are among the most intensely studied materials in solid state chemistry and physics, as they exhibit fundamentally interesting chemical and physical properties [19]. The basic perovskite structure, ABX_3, as illustrated in Figure 2.2a, has a large cation at a twelve-coordinated A site, a smaller cation at the octahedrally-coordinated B site, and an anion X. In the case of oxide perovskites, oxygen is placed at the X-position. The octahedra of B-site cations and surrounding anions form a network of corner-sharing octahedra, where the voids are filled with the A-site cations as seen in Figure 2.2b. These octahedra can tilt, expand or contract in order to compensate for non-ideal ionic size ratios in the perovskite. This makes it possible to accommodate almost all of the elements in the periodic table in the perovskite structure, hence allowing for the wide range of properties [19].

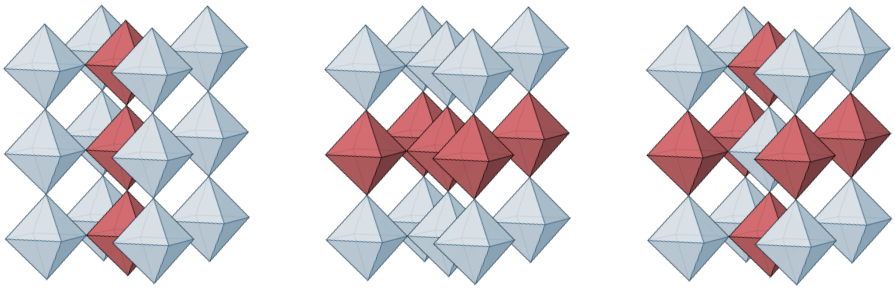

Figure 2.3: Illustration of B-site cation ordering in a) column, b) layer and c) rock-salt configurations. Each B-site cation is illustrated with colored octahedra, for simplicity, the individual ions are not included.

2.2.2 Double perovskites

Partial cation substitution is a common method to tailor the properties of a perovskite compound. The substitution can be done with the A-site cations, B-site cations, or both combined. In the case of partial B-site substitution of exactly half of the B-site cations, the cations, B' and B", can remain disordered with random distribution in the crystal structure, or they can order to form a so-called B-site ordered double perovskite, $A_2B'B''X_6$. In this case, the B-site cations can order (1) in columns, (2) layers, or (3) alternating in all three directions, as in a rock-salt-type arrangement as shown in Figure 2.3. Among these, rock-salt-ordering is the most commonly observed due to the energetical favourability, where cations of different valences alternate through the structure and minimize the electrostatic potential [19].

B-site ordering in bulk is driven by the energetic favourability of the ordered state [20]. The first driving force to be considered, is electrostatics, where the difference in the valence of the B cations, ΔZ_B, plays an important role. This is described by $\Delta Z_B = |Z_{B'} - Z_{B''}|$, where $Z_{B'}$ and $Z_{B''}$ are the ionic charges of the respective cations. The larger the B'/B" ionic mismatch, the higher the degree of ordering, because this maximizes the distance between cations with large valence [20]. Ksoll et al. describe that empirical studies show that double perovskites with a valence difference of $\Delta Z_B > 2$ are usually ordered, while those with $\Delta Z_B < 2$ are disordered, and both phases can exist for $\Delta Z_B = 2$ [20]. The preferred valence state of cations depend on the synthesis conditions, like temperature, growth rate and oxygen partial pressure. In addition, the A-site cation and its valence state determines the possible ordered states. For the case where A = La, La is trivalent and the possible B-site valence states are B'^{3+}/B''^{3+}, B'^{2+}/B''^{4+} and B'^{1+}/B''^{5+}. For LNMO specifically, the ordered phase is therefore found with Ni^{2+}/Mn^{4+} rather than Ni^{3+}/Mn^{3+} [21].

Next, the mismatch between cation radii R drives B-site ordering through local lattice strain [20]. The larger the mismatch $\Delta R_B = |R_{B'} - R_{B''}|$, the larger the driving force for ordering. In LNMO, Ni/Mn ordering is found for $\Delta R = |R_{Ni^{2+}} - R_{Mn^{4+}}| = 16\,\text{pm}$, which is much larger than the unordered case were $\Delta R = |R_{Ni^{3+}} - R_{Mn^{3+}}| = 4\,\text{pm}$. From an

energetic point of view, the minimal potential electrostatic energy is obtained when Ni^{2+} and Mn^{4+} are rock-salt ordered. However, this has to be compensated by the increased elastic energy of the lattice due to local strains, as the size mismatch is much larger in the ordered than the disordered state.

In the case of thin films, B-site ordering is also highly influenced by the substrate, its lattice constant and the subsequent epitaxial strain. Thin films of double perovskite LNMO is typically grown on functional oxide substrates with a perovskite structure, like $SrTiO_3$ (STO), $LaAlO_3$ (LAO) and $(La_{0.3}Sr0_7)(Al_{0.65}Ta_{0.35})O_3$ (LSAT), with lattice mismatch that induce a small tensile (STO) or compressive (LSAT and LAO) strain.

Although energetically favorable, the growth of B-site ordered oxide thin films is a challenging task [20]. As mentioned, growth conditions, including substrate temperature, growth rate and oxygen partial pressure, need to be optimized for ordering. In addition, deviations from stoichiometry, or growth-induced defects like oxygen vacancies or interstitial atoms, will favor crystallization in the disordered phase.

The crystal structure and space group of the $A_2B'B''O_6$ perovskites are tightly related to the B-site cation ordering, although the relation between symmetry group and degree of B-site ordering differs between material systems. Even though the ideal perovskite structure is cubic, BO_6 octahedra tilting and cationic displacements can cause structural distortions and hence ordering in other crystal structures. In the ideal case of a cubic rock-salt-ordered $A_2B'B''O_6$ perovskite, the unit cell is doubled in all crystallographic directions compared to a single perovskite [19].

Structure of La_2NiMnO_6

An ideally ordered La_2NiMnO_6 (LNMO) double perovskite can be described as a simple ABO_3 perovskite unit cell with alternating Ni/Mn-cations in the corners. For a long-range ordered system, the Ni and Mn sublattices are only occupied by the respective cation, while for a completely disordered system the Ni and Mn cations are randomly distributed without any spatial order. As for double perovskites in general, ordering is associated with a change in crystal symmetry [22], and in the case of LNMO, the ordered phase belongs to the monoclinic $P2_1/n$ symmetry group, while the disordered phase has the orthorhombic $Pbnm$ symmetry. In the monoclinic, cation ordered phase, the lattice parameters are $a = 5.515\,\text{Å}$, $b = 7.742\,\text{Å}$, $c = 5.46\,\text{Å}$ and $\beta = 90.04°$. In the case of orthorhombic symmetry, the parameters are $a = 5.50\,\text{Å}$, $b = 7.742\,\text{Å}$, $c = 7.735\,\text{Å}$ [22]. All lattice parameters are given for room temperature. Since the distortion from a cubic unit cell is small for LNMO, a pseudocubic average can also describe the ordered states. The lattice constants, corresponding d_{111} planar spacings and the associated expected x-ray diffraction angles 2θ are presented in Table 2.1. The monoclinic and rhombohedral structures typically coexist over a significant temperature range, including room temperature [23, 24]. When thin films of LNMO are grown on substrates that are cut along the (111)-plane, rock-salt ordering of the B-site cations corresponds to alternating layers of Ni and Mn-ions.

Table 2.1: Lattice parameters and corresponding expected x-ray diffraction angles of differnt crystals. Pseudocubic lattice constants (a_P) are from [22], while STO values are from [25].

Crystal structure	a_p	Strain on STO(111)	d_{111}	2θ
STO Cubic	3.945		2.27765 Å	39.568°
LNMO Monoclinic	3.88	0.64%	2.240 Å	40.26°
LNMO Orthorhombic	3.90	0.13%	2.2517 Å	39.944°

2.3 Preparation of STO(111) substrates

Strontium titanate ($SrTiO_3$, STO) is an oxide perovskite. It has a cubic crystal structure with lattice parameter $a = 3.945\,\text{Å}$ [25], which corresponds to a spacing between (111) planes of $d_{111} = 2.277\,65\,\text{Å}$. In the [111]-direction, it contains alternating stacks of SrO_3^{4+} and Ti^{4+} ions, with hexagonal ordering of the two-dimensional lattice that gives a three-fold symmetry of the plane as shown in Figure 2.4a and b, respectively. STO is widely used as a substrate for deposition of thin films, including LNMO, due to the close lattice mismatch that is provided.

2.3.1 Motivation to use STO(111)

During thin film deposition, the substrate surface structure provides a template for the film in terms interatomic spacing, surface topography and orientational symmetry. Thus, it is an essential parameter with a large influence on the growth mode of the film. To date, most work is performed on (001)-oriented substrates [26, 27]. However (111)-oriented substrates gain increased attention due to their polar nature, and the possibility of emerging electrical properties at the substrate-film interface [28–30]. The substrate orientation, that be (111), (001) or (110), controls the orientational symmetry of the epitaxial film, and is accordingly used as a control parameter. Additionally, the surface chemistry of the substrate is different for each orientation, which influences the charge transfer at the substrate-film interface and the bonding between film and substrate.

For the substrate to provide a good surface for perovskite growth, Blok et al. state three criteria: (1) that the substrate surface is single terminated, (2) that the surface of the substrate has a stable interface with air and vacuum without significant reconstructions, and (3) that the substrate surface has a stable interface with the film material [33]. In the case of (111)-oriented STO, none of the criteria are trivially met. Single terminated (111) surfaces are polar, either with a Ti^{4+} or a SrO^{2-} termination, which are unstable surface states that will eventually drive reconstruction of the surface. The optimal substrate surface is provided when the substrate is (1) terminated with a favorable reconstruction of the Ti^{4+}-(111) plane, and (2) has a step-and-terrace structure of one unit cell height. The first criteria ensure a homogenous surface polarization, which promotes systematic ordering of the atoms in the interface layers. Ideally, the stacking of perovskite unit cells is equal across the sample, hence the substrate should be single terminated. A completely

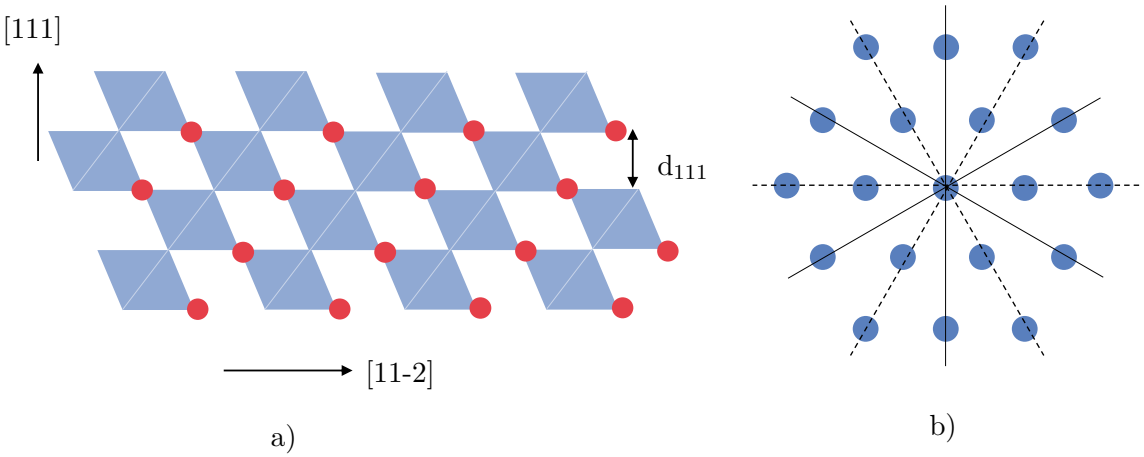

Figure 2.4: Illustrations of the structure of cubic STO. a) Side view of the crystal with the (111) surface exposed upwards. Red is Sr atoms, while blue illustrates the TiO_6 octahedra. Generated with VESTA [31]. b) Schematic of the (111) plane. Filled lines represent the hexagonal symmetry, while dotted lines represents the second order symmetries. Adapted from [32].

Ti^{4+}-terminated surface is energetically impossible to achieve, so the surface will always reconstruct, but with a stable reconstruction, the same properties can be provided. With the second criteria, the surface is atomically flat, and the only kink sites are provided by step edges, that serve as a template for film growth.

To achieve surfaces with the intended characteristics, substrates are treated in a two-step process consisting of an etching step, to remove SrO^{2-} from the surface layer, and an annealing step, to promote reconstruction of the surface to the desired atomically flat step-and-terrace structure illustrated in Figure 2.5. The ideal step-and-terrace topography has atomically defined steps with height of one unit cell, also referred to as one monolayer, and uniformly flat terraces. Surfaces where the step height is larger than one unit cell are called "step-bunched". The shape of the step edge can vary with the preparation technique, and some possibilities are illustrated in Figure 2.6. The substrates that are employed are cut on an 0.1 degree angle with a miscut of 0.5 degrees, to promote step formation.

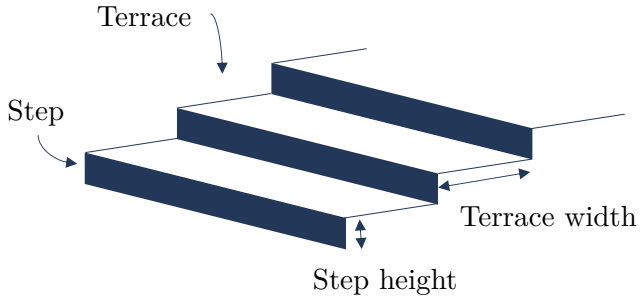

Figure 2.5: Schematic of the step-and-terrace structure of the surface, with indication of the step height and terrace width. Adapted from [32].

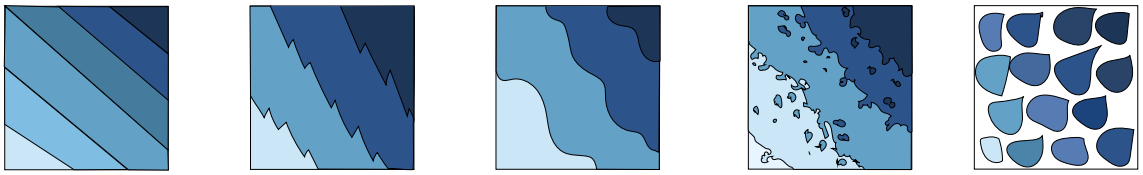

Figure 2.6: Illustration of possible structures of step edges projected in two dimensions. Straight edges are cut along one crystal direction, while faceted edges expose several crystal facets. Other morphologies, not directly related to the crystal structure, are also possible: like meandering and lace-like strep edges, and droplet shapes.

2.3.2 State of the art

Selective SrO removal by etching

Etching of STO with strong etchants, such as buffered hydrofluoric acid (BHF) is well studied, and the standard method used in substrate preparation due to the strong selectivity of HF-etchants to SrO^{2-} [34]. Etching with BHF provides a layer-by-layer dissolution of the crystal planes. In fact, SrO and other strontium compounds formed on the surface are soluble in various acids and water, while TiO_2 is stable in most acids.

Chang et al. (2008) achieved single termination for (111)-oriented STO through an etch process that combines sonication in DI water followed by buffered HF, with annealing at 1050 for 1 hour [35]. The result was atomically flat terraces, straight step edges and step heights of one unit cell. Hallsteinsen et al. (2016) compared etching with HF to etching with DI water, followed by annealing at 1050°C for 1 hour and at 1200°C for 2 hours, respectively [36]. Both procedures were performed with 5 °C/min ramp rate. The HF-based process confirmed previous work with the HF process, as it resulted in straight step edges of one unit cell height. Additionally, the work showed that the same step height could be achieved through a less hazardous process, based solely on water etching. However, the water etchant gave faceted step edges with a zig-zag pattern. By an additional rinse with DI water after annealing, single termination was also achieved through this method. Several authors have reported successful use of water etching, including [35] and [37]. Although the resulting surface structure is not as periodic as that achieved through etching with BHF, they exhibit the desired characteristics: atomically flat terraces with single termination and steps with height of one unit cell. Water etching thus shows great potential for substrate preparation of (111)-oriented STO, without the use of hazardous chemicals.

Temperature-driven surface reconstruction

The annealing process is essential to promote the formation of the desired step-and-terrace structure and stabilize the Ti-terminated surface by chemisorption of oxygen atoms [38]. Additionally, the temperature-dependent surface reconstruction process influences the final

chemical termination through progressive enrichment of Sr to the surface [39]. Annealing temperatures ranging from 900 to 1300°C have been used in the literature [35–37, 39], and variations are found in terms of the annealing time and the ramping rate. Well-defined steps and terraces can be achieved for a range of temperatures, and it depends on the interactions between the ramping rate in the oven, the maximum temperature, and the dwelling time in which the substrate is kept at this temperature. In the work of Hallsteinsen et al., annealing was performed at 1200 °C for 2 hours [36], while Chang et al. annealed substrates at 1150 °C for 1 hour [37]. These results are used as a starting point for exploring temperature and dwell parameters in this thesis.

2.4 Thin film growth

Over the last decades, new techniques for material fabrication and characterization have made it possible to develop and research non-equilibrium material phases, and strain-engineer existing materials to control their properties. This section covers the basics of thin film growth, starting with the theory of thin film growth modes, epitaxy, and effect of the substrate surface structure. An introduction is given to thin film growth by pulsed laser deposition (PLD) and in-situ growth monitoring by reflection high-energy electron diffraction (RHEED). Finally, state-of-the-art growth of double perovskites, and LNMO in particular, is covered.

2.4.1 Growth modes

Synthesis of non-equilibrium materials is easiest in the form of thin films, as their structure is highly dependent on the substrate, which allows for tuning of the atomic spacing compared to the bulk state. The growth of thin films happens by a set of processes on the atomic level: absorption, surface diffusion, nucleation and growth [40]. During absorption, ad-atoms land at the surface with a given material flux. Here, the ad-atoms diffuse along the surface or diffuse into the underlying material until they reach the location where they settle or nucleate. Kink sites on the surface can act as nucleation sites due to their increased number of dimensional "bonds" that attract the ad-atom. Following classical nucleation theory, the ad-atoms can collide and form clusters that can become nuclei for growth when they reach a certain size.

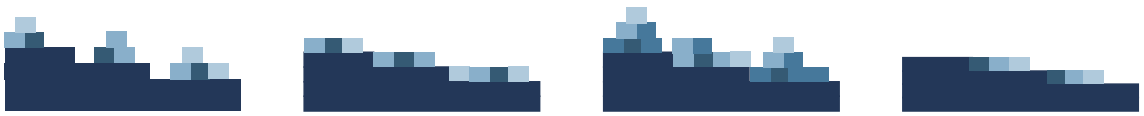

a) Island b) Layer-by-layer c) Layer-island d) Step-flow

Figure 2.7: Illustration of the modes of thin film growth on a substrate (dark blue) with step-and-terrace surface structure. The color shade of units in the film represent the time of deposition.

There are three dominating modes of thin film growth: (1) Volmer-Weber or island growth, (2) Frank-Van der Merwe or layer-by-layer growth, and (3) Stranski-Krastanov or layer-island growth [40]. Volmer-Weber growth occurs when the ad-atoms nucleate on the substrate and grow onto three-dimensional islands, driven by the selective bonding of ad-atoms to each other rather than the substrate. Frank-Van der Merwe growth occurs when the ad-atoms have stronger bonds to the substrate, than to each other. In this growth mode, the smallest nucleus grow as planar sheets. This allows for epitaxial growth and strain engineering, as the atomic spacing of the film will follow the substrate, allowing for single unit-cell level control of oxide materials [41]. Stranski-Krastnov growth is a combination of layer-by-layer and island growth, where the first monolayers are formed by layer-by-layer growth. For the following layers, layer-by-layer growth becomes energetically unfavorable, and growth of the film proceeds in the island mode.

Thin film growth can be described by a thermodynamic nucleation and growth process, as describes the growth of most material phases [40]. For the growth of thin films, the nucleation is heterogeneous and occurs at the surface, typically at step edges or defects. When the nuclei reach the critical size, the growth process continues. The growth process will depend on the kinetics of the synthesis system, like the rate of ad-atom arrival, temperature, and pressure. These variables all influence the growth process, and are used as tools for growth control, for instance to give a larger thickness before the growth mode changes from layer-by-layer to island growth.

Taking a closer look at the process of ad-atom diffusion on the surface, the diffusion process can be divided between intralayer mass transport across flat terraces, and interlayer mass transport, crossing step edges. Upward steps are energy barriers for the diffusion of ad-atoms, while downward steps represent energy sinks. Growth can also follow a fourth growth mode, namely step-flow growth, where ad-atoms diffuse to the step edges and incorporate on the lower terrace of the step edge, which has a minimal local energy barrier on the surface. For this mode, it seems like the steps only move forward as more material is deposited. A prerequisite is that nucleation predominantly happens at step edges instead of terraces, which requires the terrace width to be smaller than the diffusion length of ad-atoms, so that all ad-atoms can diffuse the required distance to reach the step edge. Figure 2.7 illustrates that step-flow and layer-by-layer growth perceives the morphology of the underlying substrate. In contrast, island growth and Stranski-Kratsnov growth lead to surface roughening.

Epitaxial thin film growth, the extended single-crystal film formation on top of a crystal substrate [41], is a tool that allows for oxide material engineering. For heteroepitaxy, where the thin film is a different material than the substrate but has a similar crystal structure, the lattice parameter of the substrate is used to guide the growth of the thin film to a given lattice parameter. Figure 2.8 illustrates strained and relaxed epitaxy. Strained epitaxy is usually observed for very thin films and is observed when the spacing of atoms in the thin film material fully matches that of the substrate. On the other hand, relaxation of the film material to its bulk structure after a critical thickness t_c, through defect introduction,

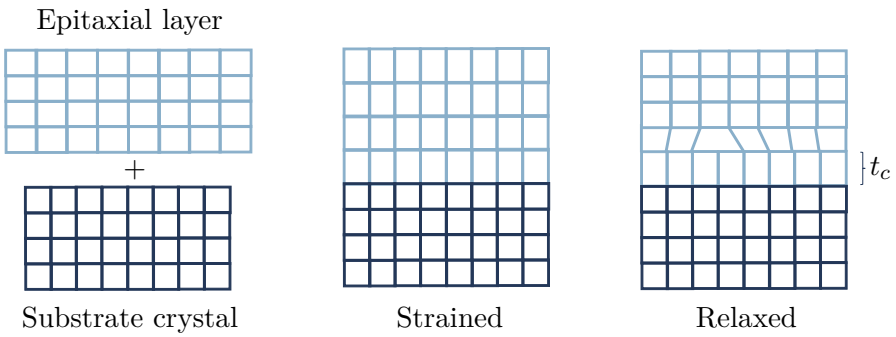

Figure 2.8: Epitaxial strain and relaxation in systems with heteroepitaxy.

results in relaxed epitaxy. This relaxation is the same as observed when growth transfers from layer-by-layer to island growth in the Stranski-Krastanov growth mode.

2.4.2 Film growth by pulsed laser deposition

Physical vapor deposition of thin films provides precise control of film growth through gradual addition of ad-atoms to a substrate. In this project, film growth by pulsed laser deposition is studied. The following section describes the working principle of deposition by the pulsed laser method, including how laser energy, deposition pressure and target-substrate distance affect the kinetic of the material plume, and how the growth through incorporation on growth sites is affected by substrate structure and temperature.

Pulsed laser deposition (PLD) is perhaps the most utilized technique for epitaxial growth of oxide thin films, due to its simplicity and flexibility in terms of deposition parameters [41]. The PLD system consists of a vacuum chamber that is equipped with pumps, a target holder that can be rotated and a substrate holder with a heating element, as well as pressure gauges and other instruments that control the deposition environment. For deposition of oxides, the chamber is held at a partial oxygen pressure and the substrate is heated to an appropriate temperature. Figure 2.9 illustrates how material is transferred to the substrate by ablation of a target with a high-energy laser. The laser pulse is rapid, typically at the scale of tens of nanoseconds, and as it is absorbed by the target material, the affected material is thermalized before it melts, vaporizes and is ionized into a highly forward-directed plasma plume that expands towards the substrate. As the plume expands, the kinetic energy of its atoms is reduced by collisions with the ambient pressure. Thus, the kinetic energy of the ad-atoms in the plume depends on the oxygen pressure in the chamber and the distance the plume travels. More specifically, higher pressure leads to slower expansion of the plume, and a reduction of the kinetic energy of ad-atoms. In contrast, longer target-substrate distance gives larger degree of thermalization, reducing the kinetic energy of the plasma. When the plasma plume reaches the substrate, the dominating growth mode will depend on the local environment on the surface. Firstly, this depends on the substrate temperature, which provides the ad-atoms with energy to diffuse on the substrate, and determines if growth happens through a step-flow growth process or through layer-by-layer growth. Next, the surface morphology, chemical termination and

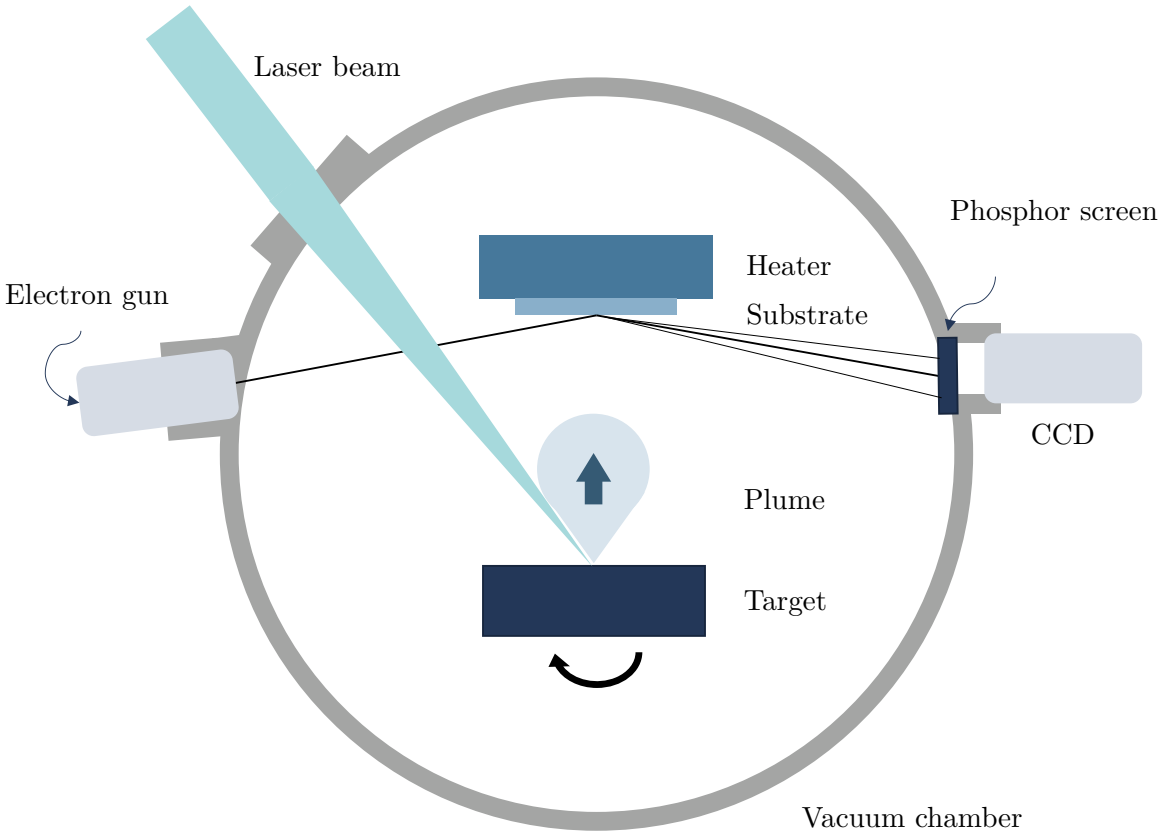

Figure 2.9: Schematic of the PLD system. Material is transferred from target to substrate by laser-induced evaporation of a plasma plume. RHEED uses an electron beam for in-situ growth characterization.

lattice parameter will determine the surface energy, thus influencing how strongly bonded the atoms are to the substrate relative to each other, and determine the growth mode as well as the epitaxy.

Typically, the amount of material introduced to the surface by one laser pulse is just a fraction of the atoms needed for growth of one monolayer, allowing for sub-monolayer control of the growth process. The interval between laser pulses is larger than the diffusion time of ad-atoms on the surface, separating the process of adding material to the surface and incorporating new material in the film. Thus, each monolayer of the film can be grown with a large degree of control, producing new, non-equilibrium states in the film.

Compared to other deposition techniques, like molecular beam epitaxy (MBE) and sputtering, PLD offers the advantages of stoichiometric material transfer, a relatively simple setup, high degree of supersaturation, and epitaxial growth. Among the disadvantages is the forward-directed nature of the plasma plume, which leads to non-uniform material deposition on larger substrates, thus reducing the potential of PLD for applications outside of research laboratories [42].

Figure 2.10: Schematic representation of the diffraction pattern observed from a (a) two dimensional and (b) three-dimensional surface. The cross indicated the position of the direct beam, which may or may not be visible in the diffraction pattern.

2.4.3 Monitoring the growth process by RHEED

Reflection high-energy electron diffraction (RHEED) can be used to characterize the crystallinity and morphology of the surface of a sample. RHEED is an in-situ technique, meaning that it is used inside the deposition chamber during growth of a thin film, and can thus be used to track the growth process and identify the growth mode while the film is deposited [43]. Figure 2.9 illustrates a basic RHEED system inside the PLD chamber. An electron beam, emitted from the electron gun, strikes the sample surface at a grazing incidence, forming a diffraction pattern from the periodic ordering of the crystal surface. The diffraction pattern is recorded by a fluorescent screen and a CCD camera. A computer program is used to track the intensity of one or more diffraction spot, and observe how the intensity changes through the growth of the film.

The shape of the diffraction pattern is related to the crystal structure and morphology of the surface. When the electron beam passes through the substrate, it is diffracted and forms a diffraction pattern, as described by the Laue condition, that gives the allowed diffraction states [44]. During RHEED characterization, the incident angle of the electron beam is small, striking the surface near grazing incidence, making the technique highly surface sensitive [45]. An atomically flat surface of a crystal can be regarded as a two-dimensional lattice, which will produce a diffraction pattern of dots in a semi-circle, as shown in Figure 2.10a. For a rough surface, the electron beam penetrates the islands that have formed rather than grazing a two-dimensional surface, and the RHEED pattern will form the rectangular diffraction pattern of a three-dimensional crystal as shown in Figure 2.10b. In the transition to island growth, the diffraction peaks are broadened in the vertical direction due to broadening of the reciprocal rods. As the surface roughens and islands are formed, the broadening continues, and additional diffraction spots are introduced. Note, however, that the diffraction pattern can deviate from perfect dots when the focus is not optimized, or following a non-monochromatic electron beam.

As the thin film grows during deposition, the intensity of the diffraction spot reduces with surface roughness, as illustrated in Figure 2.11. The intensity oscillations are related to the film growth process, and are used to measure the growth rate, if the growth is step-flow or island dominated, and if the growth occurs in one or several layers at the same time [46]. The maximum intensity indicates an atomically flat surface with complete coverage of the

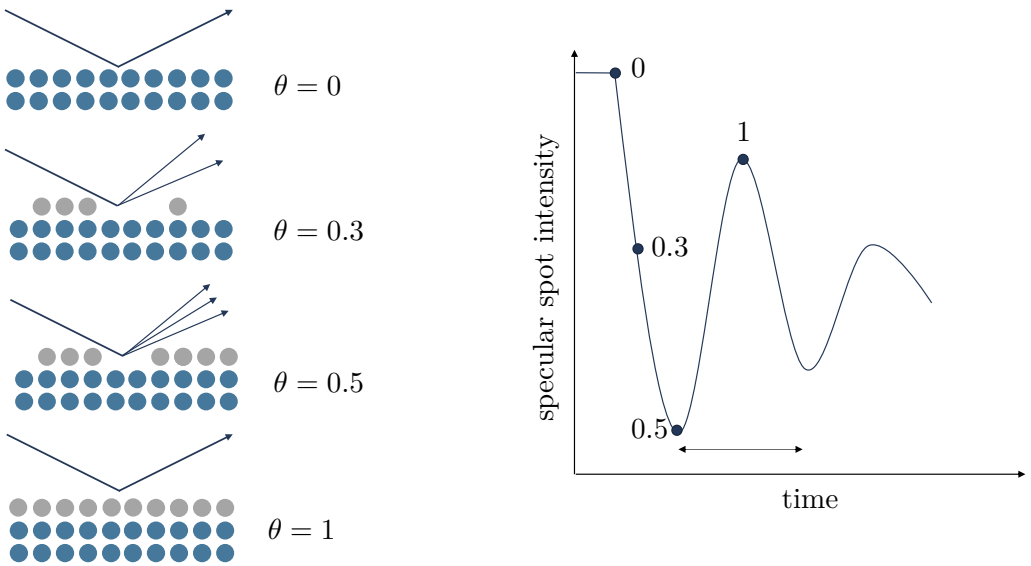

Figure 2.11: The RHEED specular spot intensity is used to monitor the growth process. Surface roughening causes the intensity to drop, and one oscillation corresponds to the complete growth of one monolayer. θ is the coverage of the top layer.

top layer ($\theta = 1$), while the minimum intensity indicates the maximum roughness between steps of full layer coverage ($\theta = 0.5$). The decrease in intensity is caused by increased surface scattering when the surface order is reduced. The period of one such oscillation can thus give the growth rate of one layer. Additionally, the intensity oscillation of the diffraction spots provides information on the growth mode of the film. In experiments, it is generally observed that the peak intensity decreases with time, because the surface gradually roughens as more atomic layers are stacked on the ideally smooth surface. This decrease in intensity is associated with a change of the growth mode from layer-by-layer to island growth [47]. For ideal layer-by-layer growth, the maxima of the intensity oscillations remain constant, as the film is just as smooth as the substrate after the completion of one layer. During step flow growth, the ad-atoms always incorporate on a step edge on the surface, so that the total surface roughness is constant throughout the growth process. Followingly, the specular spot intensity will stay constant as the film grows.

The intensity and position of diffraction peaks will change by surface roughening, which causes the pattern to change from a semi-circle to a rectangular pattern, or by a change in the crystal structure. If the crystal structure changes, for example by epitaxy relaxation, the diffraction pattern and their distance changes [45].

2.5 State of the art PLD growth of double perovskites

Not much work has been done on pulsed laser growth of LNMO thin films, but the studies that have been performed show that there is either a short-range ordered phase or coexistence of multiple phases [7]. Wu et al. (2018) and Palakkal et al. (2022) grew epitaxial thin films of LNMO on STO(001) using PLD, where advanced electron microscopy studies revealed a strain-induced monoclinic crystal structure and following B-site ordering [48, 49]. Kleibeuker et al. (2017) grew the double perovskite La_2CoMnO_6 on STO(111), which is highly similar in structure to LNMO, producing a high-quality crystal through substrate temperature of 710 °C and background pressure of 0.15 mbar during deposition [50]. Chakraverty et al. (2013) optimized the PLD growth parameters of double (for both A- and B-site cations) perovskite $LaSrVMnO_6$ in the [111]-direction, identifying high degree of B-site ordering by XRD, RHEED and TEM within the narrow window of growth conditions span by oxygen pressure $P_{ambient} = 7 * 10^{-7}$ Torr for temperature T between 960 and 1000 °C. Hallsteinsen (2012) found that the growth mode of perovskites in the [111]-direction is unstable, and that reduction of the deposition temperature to 500°C during growth of double perovskite $La_{0.7}Sr_{0.3}MnO_3$ on STO can delay the critical thickness, and stabilize layer-by-layer growth [32].

Looking more specifically at growth of LNMO, the main work is performed by Singh et al. (2009), who grew LNMO on STO(111) for a variety of deposition parameters, with temperatures from 450 to 850 °C and pressure from 100 to 900 mTorr [22]. Through polarization-dependend Raman spectroscopy and XRD, they found a well-ordered monoclinic phase in films deposited at $T = 800$ °C and $P_{ambient} = 800$ mTorr.

So far, all discussed work has utilized a single stoichiometric target for material deposition. In contrast, Ksoll et al. deposited ordered LNMO thin films by deposition of LNO/LMO superlattices on STO(111) [20]. By alternating between deposition of LNO and LMO by pneumatic nozzle spraying, films were grown in an even more controlled manner by individual deposition of the LNO/LMO layers, which showed to combine to a single ordered LNMO phase when deposited as 2/2 and 1/1 superlattices. Although not a PLD procedure, this illustrates how target switching could be used to increase the control of ordering of the LNO/LMO layers that are present in an ordered (111)-oriented LNMO phase. Although interesting, this has not been reproduced in the work of this thesis as it requires continuous switching between LNO and LMO targets, which the utilized PLD system is not optimized for.

2.5.1 Ferromagnetism in LNMO

Bulk LNMO is ferromagnetic, with a near-room temperature Curie temperature of $T_c \approx 280$ K and saturation magnetization of 5 μ_B/f.u. in bulk [49]. The magnetic ordering of LNMO originates from indirect exchange interactions via the oxygen atoms, working as exchange bridges between B-site cations. In particular, superexchange interactions lead to

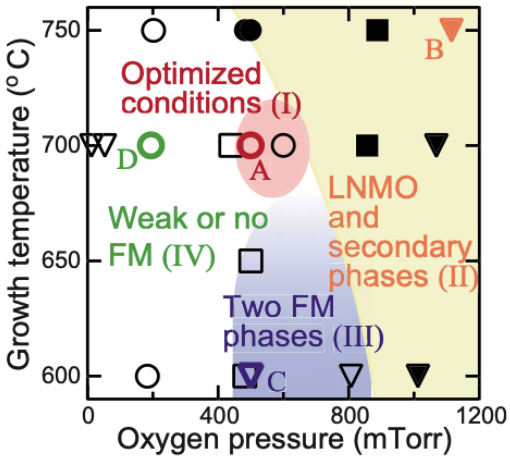

Figure 2.12: Mapping of crystal qualities and magnetic properties of LNMO depending on the growth temperature and oxygen pressure during deposition, performed by Kitamura et. al [53]. Circle, square and triangle symbols denote high, moderate and poor crystal qualities respectively. Filled symbols and open symbols represent presence or absence of seconary phases. From [53].

anti-ferromagnetic ordering while double-exchange interactions give ferromagnetism [51]. The ferromagnetic exchange interaction happens between Ni-O-Mn ions [52], both Ni^{2+}-O-Mn^{4+} with $T_c \approx 280$ K and lower temperature Ni^{3+}-O-Mn^{3+} exchange with $T_c \approx 100$ K [53]. Additionally, anti-ferromagnetic Ni-O-Ni and Mn-O-Mn exchanges can occur in disordered regions.

As the type of magnetic ordering is decided from the valence state of cations in the structure, it will be affected by the oxygen content and stoichiometry, which to a large extent determines the valence of ions. Thus, magnetic ordering requires a stoichiometric material, which is achieved through tuning of the deposition conditions, and especially important are the deposition temperature and oxygen pressure during deposition. Highly related, the magnetic ordering will follow the crystal structure of the material, as the magnetism in LNMO originate from exchange interactions between Ni-O-Ni, Mn-O-Mn and Ni-O-Mn, and the amount of each interaction type is a result of the crystal structure.

Kitamura et al. grew LNMO thin films on STO(100) by PLD, and mapped out the crystalline qualities and magnetic properties in relation to growth temperature and oxygen pressure [53]. The results were divided into four regions, as displayed in Figure 2.12. (1) At high temperature and high pressure, the films have a large amount of La-deficiencies, which may induce formation of secondary phases. The resulting films are ferromagnetic, but with lower saturation magnetization and transition temperature. (2) Low temperature and relatively high oxygen pressure resulted in two different ferromagnetic phases with T_c at 280 K and 130 K. They hypothesize that the growth temperature is too low to promote rock salt ordering of Ni and Mn ions, which gives local domains where magnetism originates from Ni-O-Ni and Mn-O-Mn interactions. (3) Low oxygen pressure results in oxygen vacancies, making the crystal lack the oxygen atoms necessary for Ni-O-Mn ex-

change interactions. Thus, LNMO exhibits weak, or no, ferromagnetism. (4) The optimal ferromagnetic properties are achieved within a narrow parameter window of temperature and pressure, where the formation of B-site cation disorder and oxygen vacancies are suppressed, so that Ni^{2+}-O-Mn^{4+} interactions are stabilized.

Similarly, Palakkal et al. studied the effect of oxygen defect engineering in LNMO thin films, and related control of their magnetic behavior [49]. Films were oxygen-deficient after PLD deposition at $P_{ambient}$ = 500 mTorr. Subsequent post-deposition oxygen annealing was performed and showed a decrease in oxygen vacancy concentration that gave a reduction in the out-of plane lattice parameter, from 7.78 Å as-deposited to 7.73 Å after 95 minutes of annealing, as well as a reduction of the saturation magnetization from 4 μ_B/f.u. to 2.5 μ_B/f.u. and a hardening of the magnetic state. This illustrates the importance of stoichiometry on magnetic properties, which can also be obtained through post-growth annealing in high-pressure oxygen.

In summary, the crystal structure, stoichiometry and magnetic state are closely related. Defects, cation valences, and arrangement of B-site ions significantly depending on the synthesis conditions, strongly influence magnetic properties [53]. To illustrate the relation, an increase of the oxygen pressure during deposition reduces the amount of oxygen defects, altering the valence state of cations, thereby changing the magnetic interactions together with crystal structure, as differently ordered states will be energetically favorable. Due to the complex interplay between deposition conditions and their effect on crystal structure, stoichiometry and magnetic ordering, optimization is far from straightforward.

Chapter 3

Experimental procedures

3.1 Substrate preparation

Table 3.1: Overview of parameters for substrate preparation. The water purity, annealing temperature and dwell time has been varied in each tested series. The name of the samples are based on the parameters that are used during substrate treatment, as follows: etchant-temperature-time.

Series	Etchant	Temperature [°C]	Time [h]	No of samples
DI-1150-2	DI	1150	2	5
DI-1150-1	DI	1150	1	4
DI-1125-2	DI	1125	2	3
DI-1125-5	DI	1125	5	1
UP-1125-2	UP	1125	2	1
T-1125-2	Tap	1125	2	1

Substrate preparation was performed to achieve atomically flat and single terminated surfaces of (111)-oriented $SrTiO_3$ (STO) with a step-and-terrace structure for further PLD deposition. (111)-oriented STO substrates (from SurfaceNet GmbH and Shinkosa) with one side polished and a 0.5 degree miscut angle were used. Some of the substrates were cut using a diamond wire saw (Well 3500 Premium) to cut each 10×10 mm substrate into 5×5 mm pieces.

The substrate preparation procedure consists of three steps: cleaning, etching and annealing. In this work, the etching chemical and the annealing parameters were varied to assess their effect on the surface structure. The following experimental procedure describes the general method that has been used, and the reader is referred to Table 3.1 for the specific method used in each substrate series.

First, the substrate was cleaned by submersion in acetone for 5 minutes, followed by submersion in ethanol for 5 minutes. Next, the substrate was submerged in de-ionized (DI) water at 70 °C under sonication in a pre-heated ultrasonic bath for 30 minutes.

Table 3.2: Overview of samples grown to assess the influence of target-substrate distance on the initial growth mode. All films were deposited by 500 laser pulses, and the sample name describes the associated distance for each film.

Sample	Target height [mm]	Substrate height [mm]	Assumed distance [mm]
D-35	82	38	35
D-40	79	36	40
D-43	75	37	43
D-46	70	39	46

Compressed air was used to blow off excess liquid after each solvent step. Finally, the substrate was annealed in a tube furnace oven (Entech tube furnace) to evaporate all residue of solvents and promote the surface reconstruction necessary for formation of the uniform step-and-terrace structure. In the tube furnace, the temperature was gradually increased from room temperature to the annealing temperature at a rate of 3 °C/min. When the annealing temperature was reached, the oven was fixed at this temperature for the annealing time, before the temperature was decreased at the same rate. The oven was operated with a constant supply of oxygen gas at 1-2 bubbles per second to provide sufficient oxygen supply to the surface during annealing.

3.2 Film growth

In this work, La_2NiMnO_6 (LNMO) thin films were grown on (111)-oriented STO substrates by pulsed laser deposition in the Mantis Deposition system (PLD lab, FACET, NTNU). A stoichiometric LNMO target was ablated with a KrF excimer laser with wavelength $\lambda = 248$ nm and fluency 1-2 J using a pulsing frequency of 1 Hz. The laser was operated in energy-constant mode. Films were deposited at 500°C in 0.11 mbar (0.10 - 0.133 mbar) of oxygen ambient with laser energy set to 300 mJ. After deposition, the films were cooled to room temperature and kept in a high-pressure oxygen atmosphere of 100 mbar (55.5 - 99.0 mbar) for 1 hour.

Table 3.3: Overview of samples grown to asses how the growth mode evolves with film thickness. Note that sample T-500 is the same as sample D-35 presented in Table 3.2.

Sample	Pulses No.	Assumed distance [mm]
T-500	500	35
T-1500	1500	44
T-2000	2000	36
T-4000	4000	39

The target-substrate distance and the growth duration were intentionally varied between depositions to assess their influence on the growth mode. Four films were grown by 500 pulses, changing the distance, as described in Table 3.2. Additionally, films were grown with a gradually increasing number of pulses to assess how the growth mode changes as the film thickens, as presented in Table 3.3. For this growth series, the target-substrate distance was changed slightly between depositions to ablate a new area of the target for each deposition. Note that sample D-35 and sample T-500 is, in fact, the same sample. One extra film, sample X-1, was grown separately from the distance- and thickness series. This sample was grown by 1500 laser pulses. For all fabricated samples, other deposition parameters were only varied when required by the PLD system. A more extensive overview of deposition parameters can be found in Table A.1 in Appendix A. The growth process of each film was monitored by in-situ RHEED, using a voltage of 24-25 kV and a current of 1.45-1.55 A.

3.3 Characterization

3.3.1 Atomic force microscopy

The surface topography of substrates and films was characterized by atomic force microscopy (AFM). All topography characterization was performed on the AFM Dimension Icon (Bruker, NTNU Nanolab), using the ScanAsyst mode and a ScanAsyst Air probe with a silicon tip with radius 2 nm, on a nitride lever with resonance frequency 70 kHz and spring constant 0.4 N/m. The ScanAsyst mode combines tapping and contact mode, and automatically optimizes scan parameters such as feedback gain, amplitude setpoint and scan rate for high-quality imaging [54].

Every sample was imaged on at least three regions, to cover a representative area of the surface. AFM is a local imaging technique where only a small area of the sample is imaged during each scan, and it is thus necessary to inspect several areas. For each new area that was studied, an overview image with dimensions 10×10 µm was first gathered. Based on these overview images, regions of particular interest were imaged with higher magnification. The regions of particular interest could be regions that are representative for the area, or that show specific details that are hard to measure with lower magnifications.

The collected images were processed and analyzed using the Gwyddion software [55]. Image processing consisted of performing a set of procedures. First, the surface leveling function was used to compensate for potential tilt of the sample during measurements. Second, the sample was leveled to make facets point upwards to increase the visibility of the step-and-terrace structure. Third, row alignment was performed to compensate for jumps that the AFM occasionally does when moving to a new row in the scan pattern. Next, horizontal scars were corrected to compensate for lost data in the measurements, which

can appear when large and sudden surface features cause drastic changes in cantilever deflection. Lastly, three points were placed on the same plane surface to level the data to terrace planes.

The resulting images were used to identify different surface morphologies and to quantify a set of surface parameters. The surface parameters of interest were the step height, the terrace width, and the terrace roughness. The step heights and terrace widths were measured across a representative region of the sample to gather information about the trend in step bunching and terrace ordering. Surface roughness measurements were performed on individual terraces using the *statistical quantities* tool and the mean square roughness (RMS) quantity S_q [56]. Roughness measurements were performed on both substrates and films to compare the roughness parameter before and after film deposition.

3.3.2 Lateral force microscopy

Surface termination was assessed by lateral force microscopy (LFM) on one of the samples in the DI-1150-1 series. The measurement was performed on the AFM Dimension Icon (Bruker, NTNU Nanolab), using the Lateral Force mode and a CONTV-A tip with tip radius 8 nm, resonance frequency of 10 kHz and spring constant 0.2 N/m. The sample was scanned in two different areas where height and lateral force data was collected. The height data was processed in Gwyddion as described for general AFM imaging. Data from height and lateral force channels were combined into a single picture in Microsoft Office PowerPoint to identify if any regions of changed lateral force originated from material contrast.

3.3.3 X-ray diffraction

X-ray diffraction (XRD) and x-ray reflectivity (XRR) measurements were performed at the XRD labs of the department of material science (IMA) and the department of electrical engineering (IES). As strain will shift the reciprocal lattice points of the film, several scan types were performed to uncover and separate the lattice parameter of substrate and film. More specifically, $\theta - 2\theta$ scans were performed in the area covering the (111) to (222) diffraction peaks of STO, around the individual diffraction peaks of (111) and (033). Additionally, detector scans were performed around the (111) and (222) diffraction peaks. A rocking curve was also performed around the (111) peak of the film. An XRR scan was performed to measure the film thickness. The presented data was collected in collaboration with senior engineer Tron Arne Nilsen and associate professor Ingrid Hallsteinsen.

3.3.4 Raman spectroscopy

Raman spectroscopy was performed using a WITec Alpha 300R confocal Raman imaging system. The Raman spectra were collected using a 532 nm excitation wavelength with 17 mW power, integration time 3.0 s and 10 accumulations using the *acc single spectrum*-command. The objective was 50x HD with 1.00 mm working distance, and the angle between the incident light beam and the sample surface plane was 90°.

3.3.5 Transmission electron microscopy

Sample T-1500 was characterized by transmission electron microscopy (TEM). Sample preparation was performed by postdoc Iryna Zelenina and Ph.D. candidate Yu Liu, where a cross-sectional TEM sample was prepared by conventional TEM sample preparation techniques and focused ion beam (FIB) lift-out. Measurements, data collection and data analysis was performed by Iryna Zelenina.

3.3.6 Ellipsometry

Ellipsometry measurements were performed together with Ph.D. candidate Stephanie Birgit Burgmann using a Woollam M-2000 Spectroscopic Ellipsometer. The ellipsometry characterization estimated the film thickness, along with the refractive index, n, and the extinction coefficient, k. First, an STO substrate was measured to have the correct optical properties to build the model. Then, measurements were performed on samples T-2000 and T-4000. The data fit was performed with the Cauchy Extended and Graded Layer models [57, 58].

Ellipsometry works by measuring the change in polarization as light is reflected of a sample surface. The measured change in amplitude and phase of light depends on the optical properties and thickness of the material in the sample. The measurements are then fitted with an optical model that uses a set of optical constants for the material system to estimate the film thickness or other properties of interest. The coherence between the measured data and the fitted model is stated in terms of the mean square error (MSE), and a model is generally considered "good" when MSE < 10. For more information on ellipsometry, the reader is referred to [59].

3.3.7 Vibrating-sample magnetometry

Vibrating-sample magnetometry (VSM) measurements were performed on sample T-2000 to characterize the magnetic properties of the deposited film. First, the samples were cut to 4×4 μm^2 pieces with the diamond wire saw. Master student Jonas Lyng-Jørgensen conducted further substrate preparation and measurements. Hysteresis measurements were performed at 50 K using magnetic field strengths from -2000 Oe to 2000 Oe.

First, sample T-2000 was measured as-deposited. Then, an additional annealing step was performed where the sample was annealed in a tube furnace at 700°C for 1 hour with an oxygen supply of 1-2 bubbles per second. The ramp rate was set to 3°C/min. VSM characterization was repeated after the additional annealing step, performing both a hysteresis measurement at 50 K and a magnetization vs. temperature measurement in the temperature range between 50 to 350 K.

Chapter 4

Results

This chapter presents the results of the performed experimental work. The chapter is divided into five sections. First, the results from substrate preparation of STO is covered. Next, the AFM-characterized surface morphology of LNMO films grown with different target-substrate distances is presented, followed by the surface morphology of films grown to four different thicknesses. The fourth section covers RHEED characterization and a study of the RHEED system. Lastly, results from characterization of the crystal structure and functional properties is presented in the final sections.

4.1 Substrate preparation of (111)-oriented STO

This section covers control of the surface of (111)-oriented STO substrates. The effect of the purity of the water etchant and the annealing temperature and dwell time on the surface structure is presented. AFM characterization showed that all methods for substrate preparation resulted in increased structural ordering compared to as-received substrates. Figure 4.1 shows the surface of an as-received substrate. Table 4.1 presents an overview of the average step heights and the range of step heights for each preparation method,

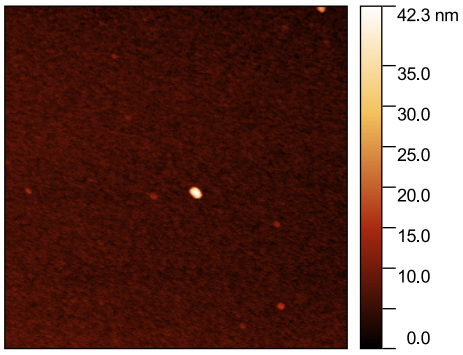

Figure 4.1: AFM image of the surface of a substrate before etching and annealing shows that the surface is unordered and with impurities. The image is $3.3 \times 3.3 \mu m^2$.

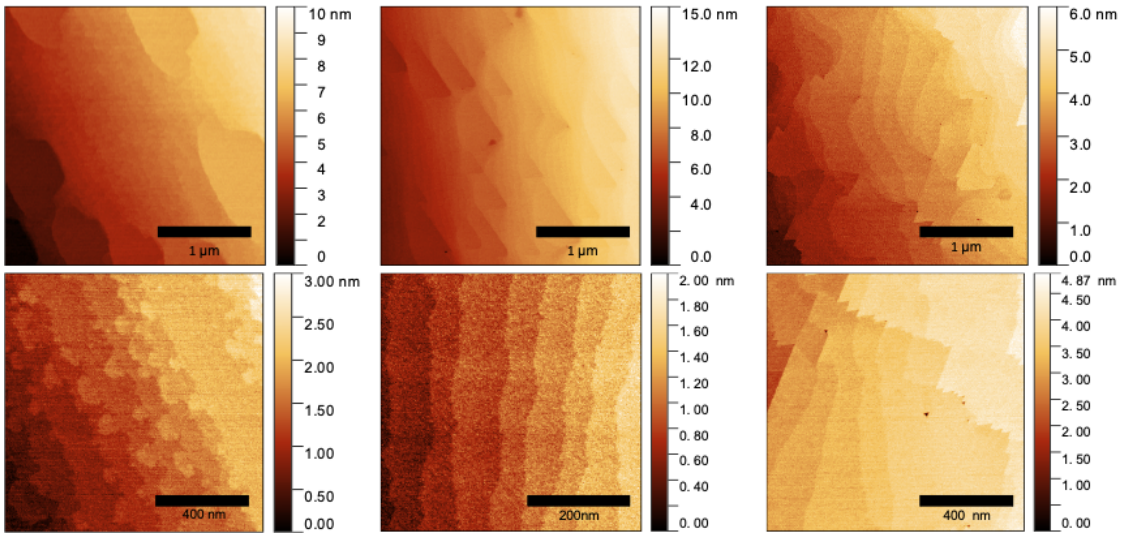

(a) UP water (b) DI water (c) Tap water

Figure 4.2: AFM micrographs of substrate UP-1125-2, DI-1125-2 and T-1125-2, prepared by use of water with different purity during the etching step. The surface of (a) and (b) have two competing configurations, one with larger, round terraces, and one with small steps which height is around one unit cell.

together with a description of the observed terrace morphologies. The reader should note that there were variations in the step heights and terrace shapes between different regions on each substrate, and between substrates prepared in the same batch. The table describes the general features for each preparation method. The step height is used to describe the step bunching. The measured step heights are both integer- or half-integer multiples of STO d_{111}, indicating that the terraces have mixed termination.

4.1.1 Effect of water purity

Three substrates were prepared by the same method, while etching with water of different purity, to observe how this influenced the final surface morphology by changing the strontium solubility. AFM characterization of the surfaces after treatment can be seen in Figure 4.2. The substrates that were etched with ultra-pure (UP) water and deionized (DI) water had similar microscopic structures, with two competing configurations on the surface: the first area-type has step-bunched, droplet-shaped terraces, while the other has a step-and terrace structure with step height of 0.5-1.5 monolayers. The height difference between droplets and the surrounding is between 1 and 2 nm. Despite the similarity in microscopic structure, high-magnification AFM imaging reveals that the morphology of the step edge is different depending on the water purity. The step edges are straight on DI-1125-2, while they are less continuous and resemble more of a lace fabric on UP-1125-2. Etching with tap water did also result in increased surface ordering compared to as-received substrates, with a combination of straight and meandering step edges.

Table 4.1: The prepared substrates had variations in terrace morphology as well as step height. Step heights are given by average and the range of heights.

Series	Step height [nm]		Morphology	No samples
	Average	Range		
DI-1150-2	0.80	0.10-2.69	Step bunching , straight	5
DI-1150-1	0.99	0.11-4.19	Straight, small facets, step bunching	4
DI-1125-2	1.63	0.25-5.97	Droplets, straight	3
DI-1125-5	0.89	0.22-1.55	Faceted	1
UP-1125-2	0.62	0.10-1.5	Droplets, lace	1
T-1125-2	0.31	0.07-0.98	Faceted, droplets	1

4.1.2 Effect of annealing temperature and dwell time

Substrates were prepared by DI-water etching, and annealed with temperatures from 1125°C to 1150°C and dwell times from 1 hour to 5 hours. The surface topography was imaged by AFM, and a selection of the obtained images can be found in Figure 4.3.

Substrates annealed at 1150 °C for 2 hours gave different results from substrate to substrate. However, they can be divided into two categories: one is highly step-bunched with visible grow-together of steps and step heights from one unit cell to several nanometers (Figure 4.3g-i), while the other has a more uniform structure with step heights ranging from 0.23 nm to 1.40 nm (Figure 4.3g). The variation in the resulting substrate structure suggests that the substrate is in a transitioning stage, where the surface configuration transitions from steps with a height of a couple of unit cells, to a structure with more step-bunching and step heights of several nanometers.

Substrate annealing at 1150 °C for 1 hour resulted in a more defined step and terrace structure where the step height ranged from one unit cell to 5 unit cells (0.22 nm - some above 1 nm). The distribution of step heights was relatively uniform, with a slight favoring of unit cell high steps. For this preparation method, the surface height profile was consistent across the observed surface regions and the prepared substrates. The terrace shape was observed to be straight, with some faceted edges that were primarily observed in the transition between terraces of different heights, as seen in Figure 4.3d. On one of the three prepared substrates, the shape of the terraces was more round, a bit broader, and with a region of gradual height increase between the free-floating terraces, as seen in Figure 4.3e.

Next, annealing of substrates at 1125 °C for 2 hours resulted in a surface structure with a combination of two surface configurations as seen in Figure 4.3a-b and Figure 4.2b. In the collected AFM images, droplet-shaped terraces are observed, with step heights between 1 and 2 nm. Between these terrace regions, are regions of gradual height increase with a

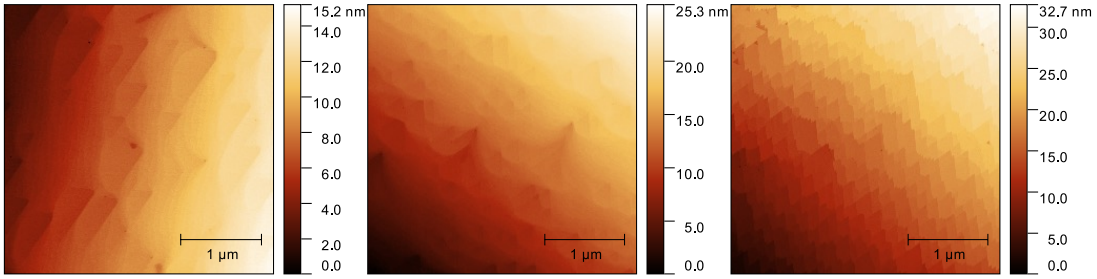

a) 1125°C 2h b) 1125°C 2h c) 1125°C 5h

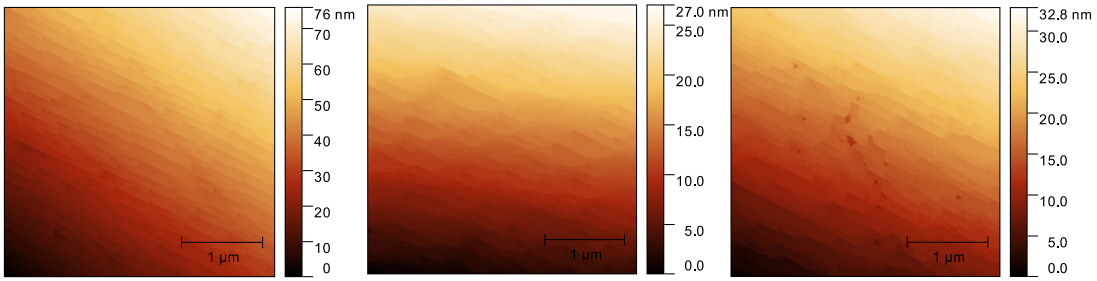

d) 1150°C 1h e) 1150°C 1h f) 1150°C 1h

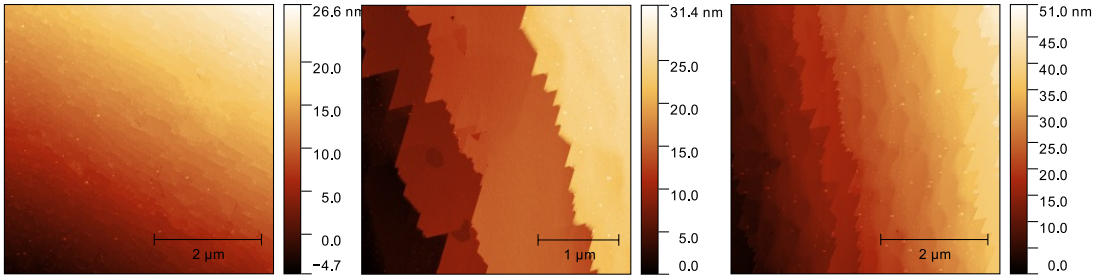

g) 1150°C 2h h) 1150°C 2h i) 1150°C 2h

Figure 4.3: Results of different substrate preparation procedures.

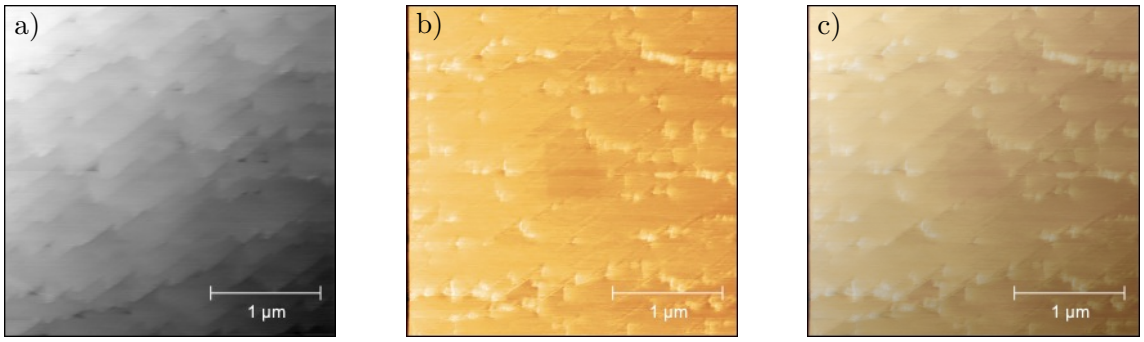

Figure 4.4: LFM image of a substrate in series DI-1150-1, consisting of signal from (a) the height channel, (b) the lateral channel, and (c) the two combined. The lateral contrast is seen by difference in yellow shading, and contrast is observed at faceted step edges. All images are 3.3×3.3 µm^2.

step-and-terrace structure. The terrace edges are wavy, and the step height varies from half a unit cell to several unit cells.

Finally, annealing of substrates at 1125 °C for 5 hours was tested, aiming to observe what influence dwell time has on the final surface structure. The substrate has a surface structure with a zig-zagged, faceted edge, as seen in Figure 4.3c, and the step height varies from one unit cell to several nanometers. The structure is consistent across the inspected areas, but shows large local variations from terrace to terrace.

4.1.3 Lateral force microscopy

Results from lateral force microscopy imaging of a substrate in series DI-1150-1 can be seen in Figure 4.4. The topography image show a step-and-terrace structure with slightly faceted step edges. For the images with frictional contrast, the contour of the same step edges are visible as diagonal lines. In addition, there is frictional contrast on the faceted step edges, apparent by the lighter yellow color. Further, darker shaded areas are observed, as in the center of the image. When combining the signal from vertical and lateral channels, it is prominent that the frictional contrast is primarily found on the terrace edges, where the frictional properties are different due to the steps. Additionally, the frictional contrast is similar between terraces, indicating that the observed terraces have the same termination.

4.2 Effect of target-substrate distance on initial film growth

During the fall semester of 2021, project student Linda Joseph performed work on pulsed laser growth of LNMO thin films in the same deposition chamber. Then, RHEED oscillation patterns indicated that the target-substrate distance should be at a minimum to provide optimal conditions for layer-by-layer growth [10]. For the work of this master thesis, the distance between the target and the substrate was varied to observe how target-substrate distance influences the initial growth mode. Four films were deposited by 500 laser pulses, with similar deposition parameters, except for the target-substrate distance, which is intentionally varied. Additionally, the substrate surface morphology differed between samples, which also influenced the growth mode.

Here, the growth mode is evaluated by AFM characterization of the film surface roughness on flat terraces. In Table 4.2, the roughness of the terrace is compared to that observed on the substrate before deposition to evaluate if film growth has increased the roughness. Roughness measurements are performed on flat terraces, and in areas of gradual height increase that are sometimes found on the surface. These are denoted area A and area B, respectively, as indicated in Figure 4.5b. AFM micrographs of the thin film surfaces, grown with target-substrate distance of 35 mm, 40 mm, 43 mm and 46 mm, are presented in Figure 4.5 along with AFM images of their associated substrate surfaces. For all samples, the surface structure is intact from substrate to film without any large degree of roughening through island formation.

For D-35 (Figure 4.5a), the observed surface roughness (RMS) decreased from 300 ± 164 pm on the substrate to 166 ± 75 pm on the film. Similarly for D-40 (Figure 4.5b), the topography is conserved. This substrate had some flat regions, and some regions of gradual height increase. The film has similarly flat regions as the substrate, while the regions of gradual height increase have the same roughness. For D-43 (Figure 4.5 c), the topography of the surface has changed from a mixture of meandering and straight steps on the substrate, to rounder areas on the film surface. These round areas follow the step structure of the substrate and are anchored to a step site. In inspected areas, they are 4-5 monolayers high, while the steps are bunched with a step height of 10-15 monolayers. The

Table 4.2: RMS roughness parameters of the different films, as measured on flat terraces (Area A) and across small-stepped areas with continuous height increase (Area B). The roughness S_q is given as mean ± standard deviation.

		Area A		Area B	
Film number	Distance	Substrate (S_q, [pm])	Film (S_q, [pm])	Substrate (S_q, [pm])	Film (S_q, [pm])
D-35	35	300 ± 164	166 ± 75	-	1865 ± 612
D-40	40	166 ± 63	159 ± 36	1052 ± 787	1100 ± 443
D-43	43	118 ± 13	265 ± 95	-	-
D-46	46	239 ± 80	148 ± 48	1479 ± 163	1040 ± 154

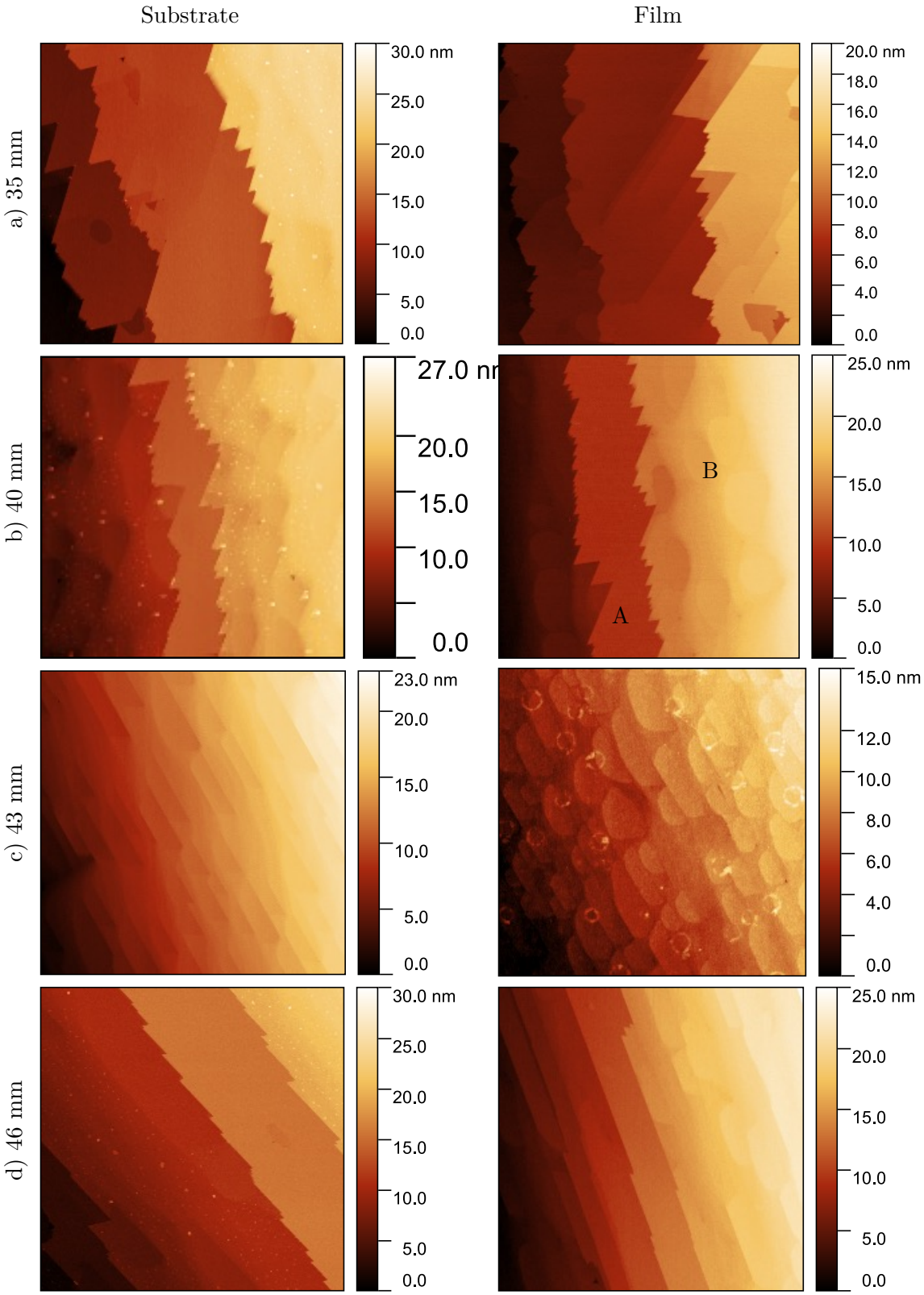

Figure 4.5: AFM micrographs of film (a) D-35, (b) D-40, (c) D-43 and (d) D-46, grown by 500 pulses with different distance between PLD target and substrate surface. All images are 3×3 μm^2, while the vertical scale varies, as indicated. For all depositions, the surface morphology is reproduced from substrate to film. Area A and B are indicated on the image of D-40.

formation of such nuclei on the terraces may indicate that the film grows by nucleation and growth mechanism that grow planar sheets on individual terraces. Finally, D-46 (Figure 4.5d) has a step-bunched substrate surface, which is reproduced on the film. The surface roughness is slightly decreased by film growth in both area A and area B. As for D-43, there are indications of a birth-and-spread growth mechanism on the terraces.

4.3 Evolution of the growth mode throughout the growth process

Films were grown to four different thicknesses to observe how the film surface structure, and hence the growth mode, evolves during film growth. This process can identify the onset of transition to an island growth mode, as it identifies when surface roughening starts. The target-substrate distance was kept within the closest half of the possible range. As it was observed in the series with varying target-substrate distance that the distance had no drastic influence on the growth mode for the first few film layers, it was not attempted to keep it constant. In the following section, it is assumed that the distance did not influence the growth mode and that the differences in surface morphology depend on substrate topography and growth length alone. AFM images of the sample surfaces, and the surface of the substrate they were grown on, are shown in Figure 4.6.

For sample T-500 (Figure 4.6a), AFM inspection shows that the film replicates the substrate surface structure in terms of the terrace widths, step height and surface of the terrace. As mentioned in section 4.2, the RMS roughness measure on terraces decreased from 300 ± 164 pm to 166 ± 75 pm through film growth. The substrate surface consisted of flat terraces, and terraces with a gradual height increase that still was rough. Note that this film is the same as described as D-35 in section 4.2.

Sample T-1500 (Figure 4.6b) was grown on a surface with step heights varying between 1, 2 and 3 monolayers and roughness of 155 ± 21 pm. The step edges had triangular shapes along them. For the film, the same step-and-terrace structure is visible. However, the step edges are less defined, and the terraces are rougher with island clusters that are 0.5-1 nm high, corresponding to 2-4 monolayers. While the islands vary in width and length, their size is limited to the terrace.

Sample T-2000 (Figure 4.6c) was grown on a surface that consisted of two very different areas. Small steps of monolayer height, with a lace-like edge structure, were accompanied by larger, droplet-shaped terraces whose width was measured to 800 nm at most. These large terraces had a roughness of 116 ± 39 pm. The film has the same two types of structures on the surface, where the large terraces have remained smooth and now exhibit a roughness of 158 ± 36 pm. As observed for T-500, there is no substantial roughening on the large terrace. On the small terrace, on the other hand, the steps have grown together and the surface has a rougher nature. It should be noted that the roughness has not been measured on these terraces, because their narrow width made it hard to

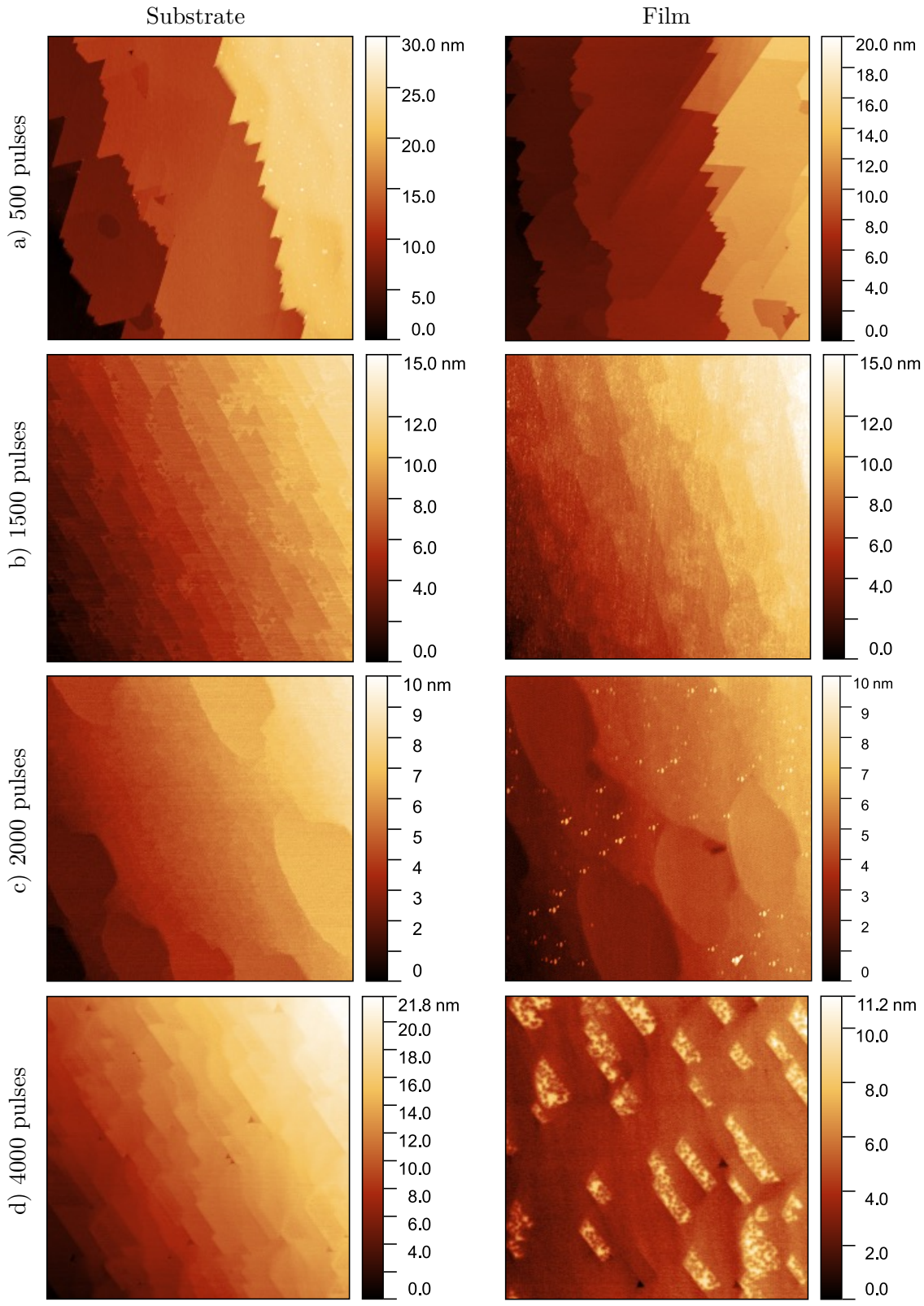

Figure 4.6: AFM images of film (a) T-500, (b) T-1500, (c) T-2000 and (d) T-4000 and the respective substrates. All images are 3×3 µm^2, height scale differs between images and is included. The substrate morphology is reproduced for all films. Film (a) has grown layer-by-layer and has smooth terraces, while (b), (c) and (d) exhibit roughening and island formation.

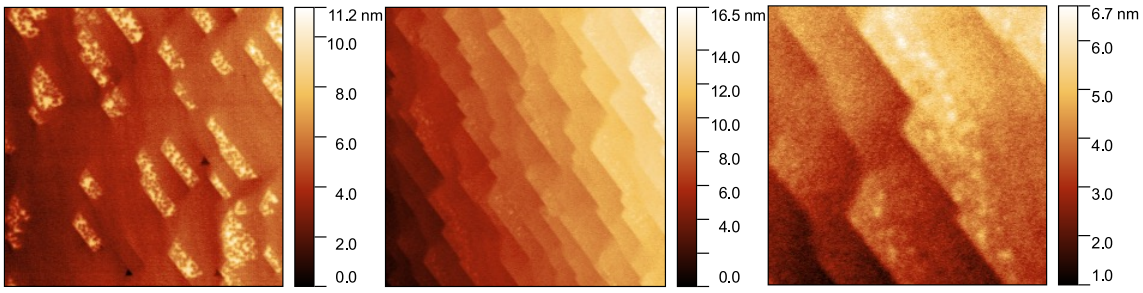

a) b) c)

Figure 4.7: AFM images of the surface of T-4000. The degree of surface roughening is large in (a), while roughening is less prominent in area (b). These images are 3×3 µm^2. Image (c) shows a 1×1 µm^2 magnification of the nuclei on terraces of (b).

Table 4.3: RMS roughness parameters of the different films and their substrates, as measured on individual terraces. The roughness S_q is given as mean ± standard deviation.

Film number	Distance	No of pulses	Substrate (S_q, [pm])	Film (S_q, [pm])
T-500	35	500	300 ± 164	166 ± 75
T-1500	44	1500	155 ± 21	458 ± 71
T-2000	36	2000	116 ± 39	158 ± 36
T-4000	39	4000	236 ± 188	608 ± 408

measure the roughness on individual terraces with the same Gwyddion-tools that were used for the other films. In addition to the grow-together of terraces, 3-5 nm high nuclei are observed. However, these nuclei have a distinct shape that is repeated across the area. Such a repeated pattern is often associated with an AFM tip artifact or dirt on the AFM tip. But, as these patters were not observed on large terraces, it is believed that they originate from actual islands and that the shape is magnified by the tip artefact.

Finally, the thickest sample, T-4000, is presented in Figure 4.6d. It was grown on a surface with step and terrace structure, with relatively straight step edges with some faceting. Some step edges are clearly defined, while others have a smoother transition between them. Figure 4.7 shows that the morphology of the film varies between inspected areas. Some areas resemble the substrate to a large extent, with the substrate structure still clearly visible, although including small islands that are 0.5-1 nm (2-4 monolayers) high and ≈ 1 nm wide and spread across the steps. In other areas, like the one presented in 4.6d, the morphology of the substrate is less obvious to spot on the film. The steps have grown together and the surface resembles more of a veil. However, the substrate morphology can be recognized in shape and the orientation of the islands that have formed on top. These follow the orientation of the steps, and the width is limited to that of the original terrace. These islands seem to consist of several islands that have grown together, as the height varies across the individual island, with the maximum height being 2-4 nm (8-16 monolayers). An overall roughening of terraces from 236 ± 188 pm on the substrate to 608 ± 408 pm on the film is measured.

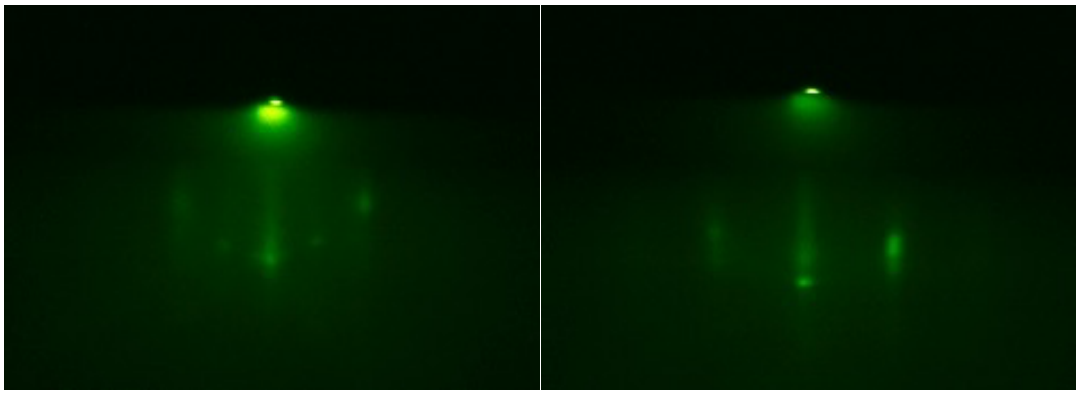

a) 30° b) 60°

Figure 4.8: Diffraction pattern of a substrate from two different azimuth angles. Diffraction from angle (a) results in five distinct diffraction spots in the semi-circle, while (b) results in three. The direct beam is visible above the semi-circle.

4.4 RHEED characterization of film growth

This section covers the work that was performed on growth characterization with RHEED. First, examples of RHEED diffraction patterns on substrates and during film growth are presented. During the work of this thesis, instabilities in the intensities of the diffraction spots were identified, and the observed effect of pressure variations and target rotation is covered in this section. After these perturbations were dampened, the RHEED intensity oscillation from film deposition was more prominent. A final intensity tracking during a deposition is shown.

4.4.1 Diffraction pattern from substrate

The diffraction pattern obtained from a substrate depends on the orientation of the electron beam relative to crystal directions in the sample. As the STO(111) surface is hexagonal, it has 6-fold symmetry that results in repetition of the diffraction pattern for every 60°. Additionally, there are symmetry axes between these with slightly different spacing between atoms, as illustrated in Figure 2.4b. Both sets of angles give diffraction patterns that can be monitored with RHEED during thin film growth. Figure 4.8 show the diffraction patterns, and the azimuth angle is rotated 30° between a) and b), corresponding to the <1-10> and <11-2> crystal directions. The diffraction spots appear not as perfect dots, but slightly streaked, meaning that the surface is not perfectly atomically flat.

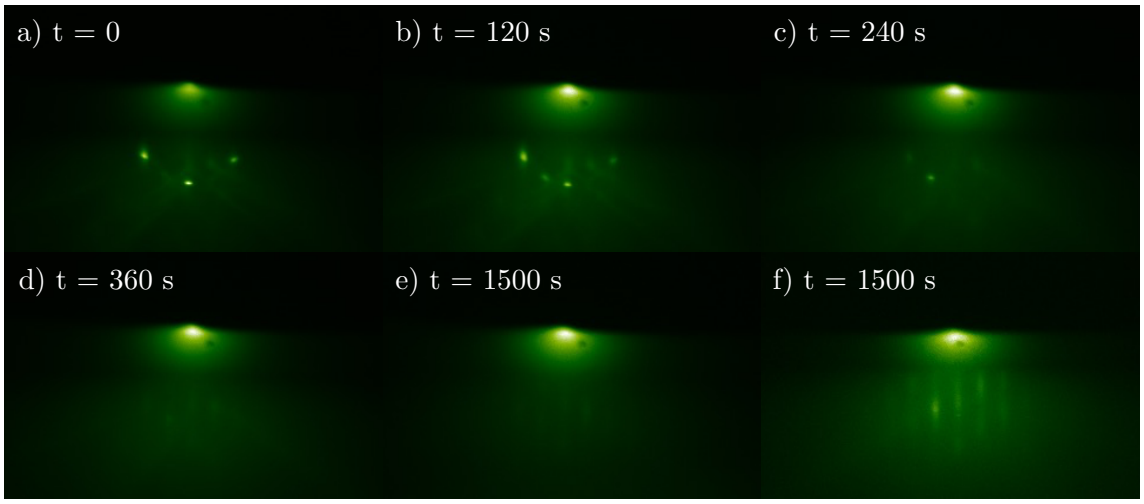

Figure 4.9: The diffraction pattern changes during deposition of thin film X-1. From the onset of deposition (a), the diffraction pattern changes from a semi-circle to a rectangular pattern through elongation and weakening of the diffraction spots. Images (a-e) are collected at the same azimuth angle, while (f) is rotated 30° relative to these.

4.4.2 Diffraction pattern during deposition

Imaging the diffraction pattern during deposition of the thin films can provide information about the crystal structure and surface roughness. Figure 4.9 shows the diffraction pattern of sample X-1 before, during, and after thin film deposition. Before deposition, Figure 4.9a, the diffraction pattern has the shape of a semi-circle with three distinct diffraction spots. During the first two minutes of deposition, new diffraction spots appear along with additional Kikuchi lines, while other diffraction spots weaken. After six minutes and throughout the rest of the deposition, the diffraction pattern has elongated spots and is barely visible. Based on what is visible, the pattern resembles a rectangular diffraction pattern. Rotation of the azimuth angle by 30° after deposition gives a brighter diffraction pattern with a clear rectangular shape that resembles a three-dimensional surface, as seen in Figure 4.9f.

4.4.3 Sensitivity of the specular spot intensity to external factors

As mentioned in Chapter 2, the intensity of the specular spot is extremely sensitive and will be influenced by thermal fluctuations, vibrations, or magnetic fields inside the deposition chamber. When the periodicity of these oscillating fields is in the same range as the periodic oscillations induced by film growth, it is hard to verify if oscillations originate from film growth. The following section presents the influence of throttle valve adjustments and target rotation on the specular spot intensity.

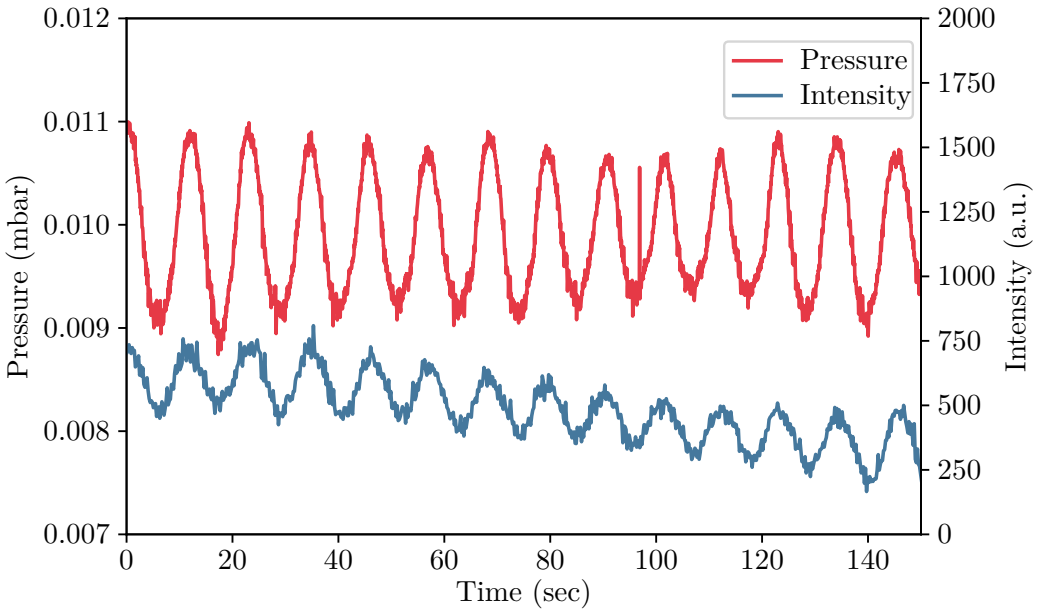

Figure 4.10: Oscillations in the background pressure inside the chamber induces oscillations in the specular spot intensity.

Pressure dependency

It was observed that the intensity oscillated following periods that corresponded to oscillations in the gas pressure. The mechanism for pressure fixation in the PLD chamber works the following way: the vacuum pumps are constantly running and pumping down the pressure. Simultaneously, the chamber has continuous input of oxygen gas. The flux of oxygen gas is controlled by a throttle valve, which opening is constantly adjusted to obtain a set oxygen pressure. The throttle valve is controlled by a feedback loop, that reduces the gas flow when the pressure is above the setpoint, and the other way around when it is below the set pressure. Because of this operation mechanism, the pressure inside the chamber constantly oscillates around the set pressure. The deviation from the optimal pressure is small, but nevertheless gives an influence on the intensity of the electron beam that can be described by scattering of the beam on the oxygen atoms, absorption, or that it causes vibrations.

Figure 4.10 displays the pressure inside the chamber and specular spot intensity when the pressure is controlled by the Titanium software (control software of the Mantis PLD system), with the pressure setpoint at 0.010 mbar. The substrate is heated as usual during deposition, the target rotation is set to zero, and there is no ongoing deposition. The pressure oscillates around the pressure setpoint with a period of 11-12 s. The intensity of the specular spot oscillates with the same periodicity. When the throttle valve is set to a fixed value, the pressure has increased short-term stability, and no such oscillations are observed for the RHEED specular spot intensity.

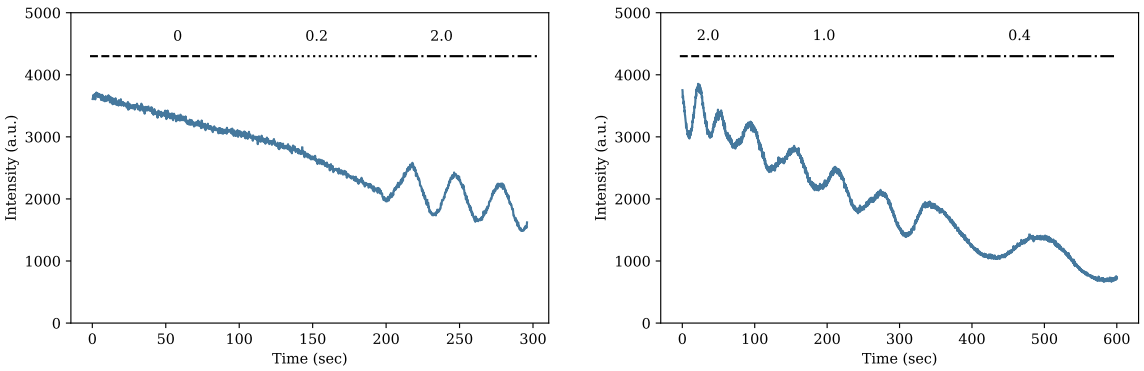

(a) (b)

Figure 4.11: The specular spot intensity is influenced by the rotational speed of the target, and the oscillation period is different for (a) no rotation, 0.2 mm rotation, 2 mm rotation, and (b) 2 mm, 1 mm and 0.4 mm.

Target rotation

Next, it was observed that the intensity of the specular spot was influenced by the rotation of the PLD target. To determine this effect, the intensity was tracked in vacuum and with different rotational speeds, as shown in Figure 4.11. First, the rotation was set to zero, and the intensity had no oscillation. No substantial difference was observed when the rotation speed was increased to 0.2 mm. However, with the target rotation set to 2.0 mm, the specular spot intensity oscillated with a period of $\approx$ 30 s. Similar behavior is observed in Figure 3, where it is seen that reduction of the target rotation to 1.0 mm and 0.4 mm decreases the oscillation period compared to rotation at 2.0 mm. In fact, the oscillation period is decreased to $\approx$ 100 s and $\approx$ 150 s for rotation at 1.00 mm and 0.4 mm, respectively.

Due to the PLD setup, the target must rotate during deposition to avoid hole-burning on the target. These oscillations demonstrate that the periodicity of the rotation-induced intensity oscillations depends on the rotation speed. For rotation speeds between 0.2 mm and 0.4 mm, as used for the depositions in this project, they do not interfere with layer-by-layer growth oscillations. However, one should be aware of the rotation-induced oscillations when RHEED data is interpreted, especially for oscillations with a periodicity corresponding to the rotation speed used during deposition.

4.4.4 Specular spot intensity tracking during deposition

Growth of sample X-1 gave visible intensity oscillations of the specular spot during RHEED as shown in Figure 4.12. This intensity tracking was performed after optimization of the RHEED conditions had been performed, including pressure adjustment and target rotation. Presence of intensity oscillations indicates a sharp interface with adequate quality. The film was deposited by 1500 pulses (1500 s), but only the first 150 seconds are shown because the signal is dampened and is low for the rest of the deposition.

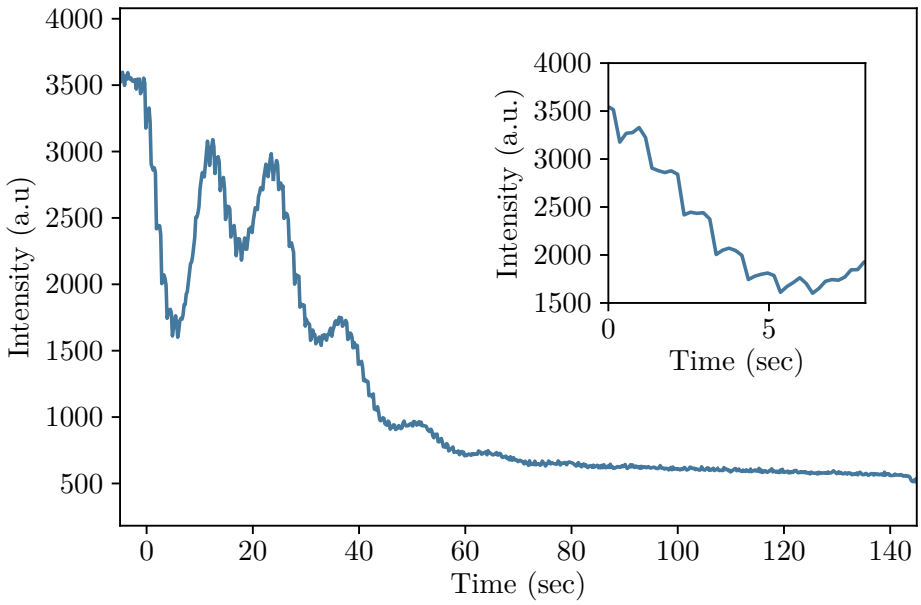

Figure 4.12: The intensity of the specular spot of the RHEED pattern oscillates as the film grows through layer-by-layer growth. The inset shows the first few seconds of deposition, where each individual laser pulse gives additional ad-atoms that influence the spot intensity.

During this deposition tracking, the intensity of the RHEED specular spot had an average oscillation frequency of 13 seconds. Assuming the pseudocubic monolayer d_{111} spacing for ordered monoclinic LNMO, $d_{111} = 0.2240$ nm, this corresponds to a growth rate of 0.172 Å/s and a film thickness of 25.8 nm after 1500 s of growth. There are five clear oscillations before the signal is dampened too much to see anything more. In the first oscillation, the intensity drops for the first six laser pulses. For the following six-seven laser pulses, the intensity increases to a new maximum. In the second oscillation, the intensity drops less with each laser pulse, and the minimum intensity is only half the way down from the bottom of the first oscillation. The second intensity oscillation has a maximum at the same intensity as the first one. The subsequent oscillation has its minima at the same intensity as the first one, and the stable maximum is just slightly above this minimum value. The signal is gradually dampened for the following three oscillations, reducing the visibility of oscillations. After approximately 400 seconds, the signal is dominated by noise, and neither the roughening from the addition of ad-atoms from individual laser pulses, nor the oscillations associated with growth of one layer, can be identified.

The specular spot intensity is altered by each individual laser pulse. Every laser pulse brings more ad-atoms to the surface. In the segment of surface roughening, these ad-atoms first deposit at a random spot on the surface, giving a significant drop in the specular spot intensity. Next, the ad-atoms diffuse on the surface and incorporate on already existing clusters, so that the degree of ordering is slightly increased, with a subsequent increase in the intensity. In the inset in Figure 4.12, it is observed that the recovery of the intensity is largest on top of the oscillation, and smaller at the bottom of the oscillation. This is because the relative roughness is largest when $\theta = 0.5$, hence the minor diffusion-induced ordering has less influence on the overall roughness.

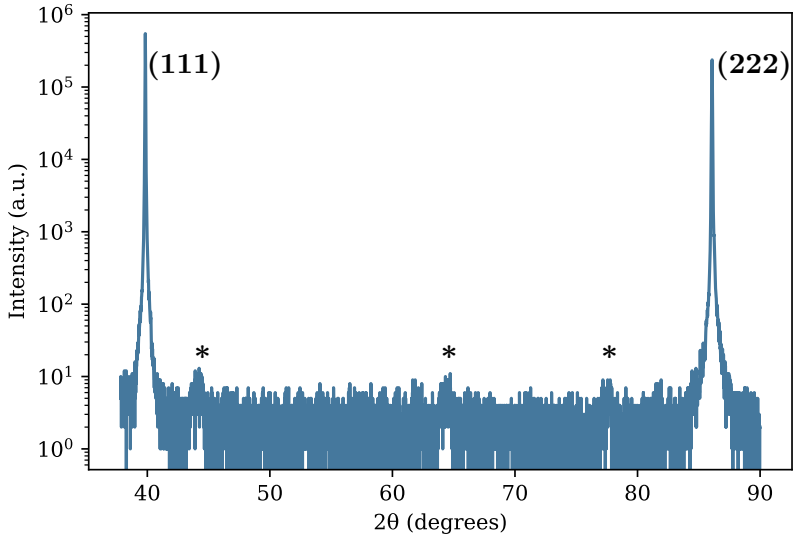

Figure 4.13: X-ray diffraction $\theta - 2\theta$ scan with two high-intensity diffraction peaks, corresponding to the (111) and (222) planes. Three additional peaks are marked by *.

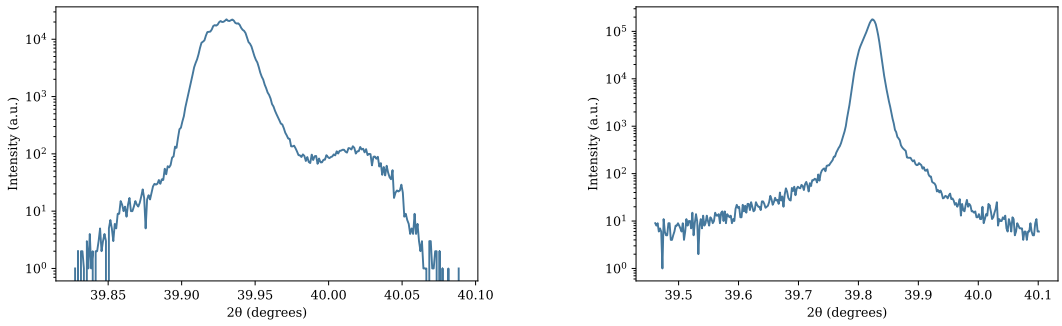

(a) (b)

Figure 4.14: Scans around the (111) diffraction peak. (a) Detector scan aligned to film, (b) $\theta - 2\theta$ scan aligned to substrate.

4.5 X-ray diffraction

X-ray diffraction scans were performed on sample T-2000 to identify the crystal structure of the film, confirm epitaxial growth, and measure the film thickness. Here, the results from $\theta - 2\theta$ scans, a detector scan and a rocking curve scan are presented. Additional $\theta - 2\theta$, detector and x-ray reflectivity (XRR) scans were performed, and can be found in Appendix B. Analysis of the XRD measurements have been difficult, as the film and substrate peaks are overlapping.

Figure 4.13 shows a $\theta - 2\theta$ scan covering the angles from the STO(111) peak to the STO(222) peak, which are the prominent peaks in the scan. Zooming in at the STO(222) peak, as presented in Figure B.1b, the substrate peak is located at 86.08° with a film peak at 86.26°. Compensating for the offset between measured and theoretically expected

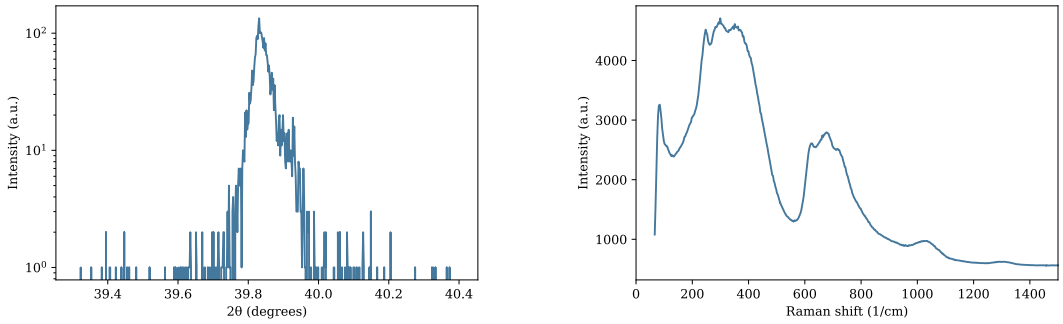

(a) (b)

Figure 4.15: (a) Rocking curve XRD-scan, aligned to the film and (b) Polarized Raman spectra from sample T-2000

values presented in Chapter 2, the film peak is located at 85.38°. Compared to bulk values, the film peak is slightly shifted, which indicates compression of the in-plane lattice parameter. Based on Figure B.2a, d_{111} is found to be 2.274 Å, compared to 2.240 Å and 2.2517 Å for monoclinic and orthorhombic unstrained LNMO, respectively. In the pseudocubic notation, this corresponds to a lattice parameter $a_P = 3.9387$ Å. In addition to the (111) and (222) peaks, extra low-intensity peaks are observed at $2\theta = 44°$, 64.4° and 77.6°, in the broad $\theta - 2\theta$ scan in Figure 4.13. These correspond to lattice spacing of $d = 2.1$ Å, 1.465 Å and 1.2423 Å. A detector scan around the (111) diffraction peak is presented in Figure 4.14a. The scan shows one peak at 39.93° and a lower intensity peak at 40.02°. For the $\theta - 2\theta$ scan around the (111) peak in Figure 4.14b an asymmetric substrate peak is observed at 39.83°, with a lower-intensity peak at the right hand side at 39.91°. For all these four scans, the substrate peak is accompanied by a film peak at higher 2θ, corresponding to smaller d-spacing. The d-spacing is larger than literature values for pseudocubic LNMO, which indicate that the film is compressively strained, following epitaxial growth. A rocking curve measurement was performed to measure the crystallinity of the film, as seen in Figure 4.15a. The rocking curve displays a central peak at 19.92° and a shoulder at 19.96°. The full-width half maximum of the peak is $< 0.2°$.

4.6 Raman spectroscopy

Raman spectroscopy was used to identify Raman-active vibrational modes in the sample, which set is characteristic for different crystal structures. The Raman spectra in Figure 4.15b is measured on sample T-2000 at room temperature. Several polarizations of the incident light were tested, and all resulted in the same spectra.

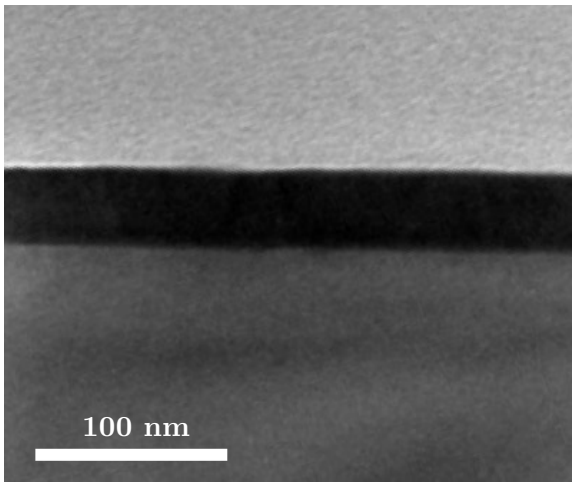

Figure 4.16: Cross-sectional TEM image of the LNMO (black) thin film, deposited on STO:Nb (dark grey) of sample T-1500. The light grey color is carbon coating, added during TEM sample preparation. Image acquired by Iryna Zelenina.

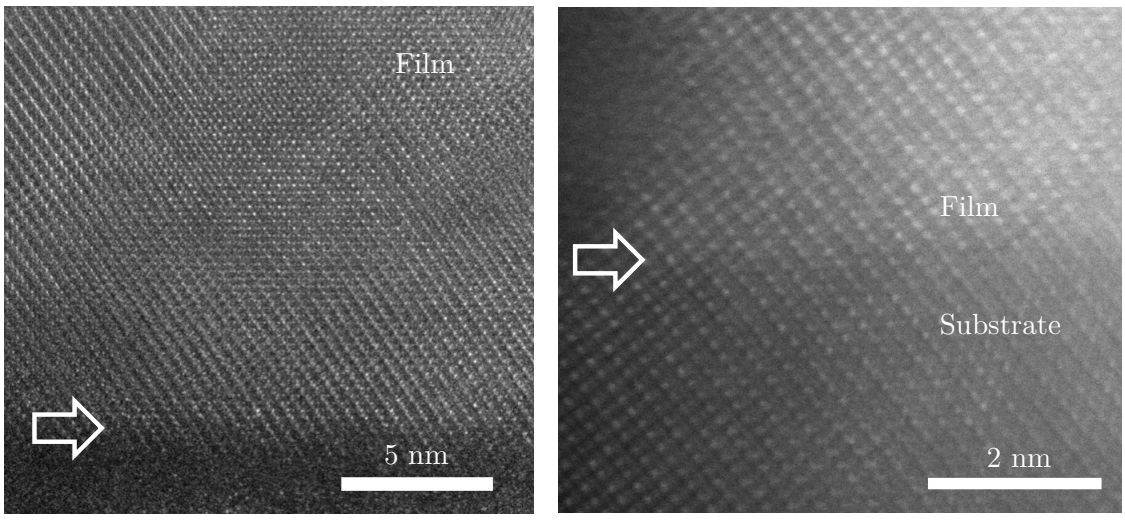

a) TEM b) STEM

Figure 4.17: Cross-sectional (a) TEM and (b) STEM imaging show that the sample is crystalline and that the stacking of atoms is similar between film and substrate. The interface is indicated by white arrows. Images acquired by Iryna Zelenina.

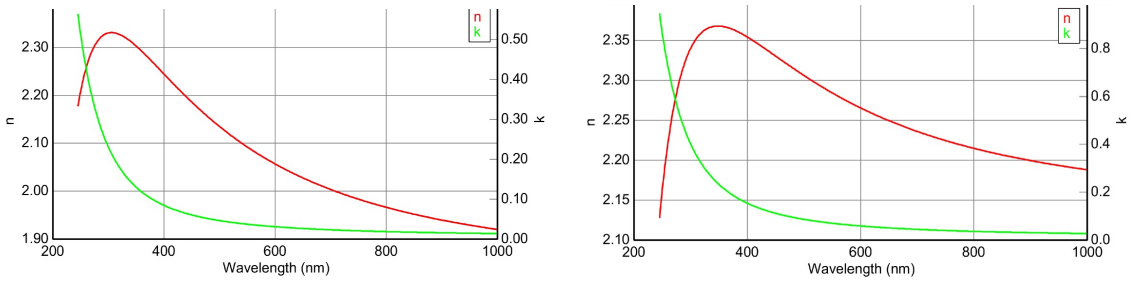

a) b)

Figure 4.18: Ellipsometry measurements on (a) T-2000 and (b) T-4000, fitted with the Cauchy Extended model, gives the refractive index n in red and the extinction coefficient k in green, as a function of wavelength.

4.7 Transmission electron microscopy

Cross-sectional TEM imaging show that the thickness of sample T-1500 is ≈ 23 nm, as shown in Figure 4.16. This corresponds to a growth rate of 0.1534 Å/s. Additionally, the TEM and STEM images in Figure 4.17 show that the film is crystalline with a sharp interface between substrate and film.

4.8 Ellipsometry

Ellipsometry is an optical technique for characterization of dielectric properties of thin films. The change in polarization of light upon reflection of the sample is measured, and compared to a model. For this thesis, ellipsometry has been used to measure the thickness and the complex refractive index of thin film T-2000 and T-4000.

For T-2000, the thickness was estimated by two different models. The Cauchy Extended model gave a thickness of $t = 24 \pm 0.545$ nm, assuming surface roughness of 0.0 nm but otherwise with free parameters. The model had a mean square error (MSE) of 37.917. Next, the Graded Layer model estimated a thickness $t = 26.22 \pm 0.742$ nm, also assuming zero surface roughness while all other parameters were free. This model had a MSE of 33.311. For T-4000, the thickness was estimated to 66.86 ± 0.424 nm when the roughness was assumed to be 0.0 nm, by a model with MSE 23.245. For the Cauchy Extended model with thickness fixed at 50 nm, the model fited a roughness of 0.51 nm, and the model had a MSE of 46.917.

Figure 4.18 shows the refractive index n and extinction coefficient k as function of wavelength, measured for films with two different thicknesses grown by 2000 and 4000 pulses. The constants are approximated using the Cauchy Extended model. T-2000 has a maximum refractive index of $n = 2.33$ at $\lambda \approx 320$ nm, which decreases in both directions. For T-4000, n reaches its maximum value of 2.37 at $\lambda \approx 370$ nm, indicating that the refractive index increases and shifts towards longer wavelengths for thicker films. The extinction

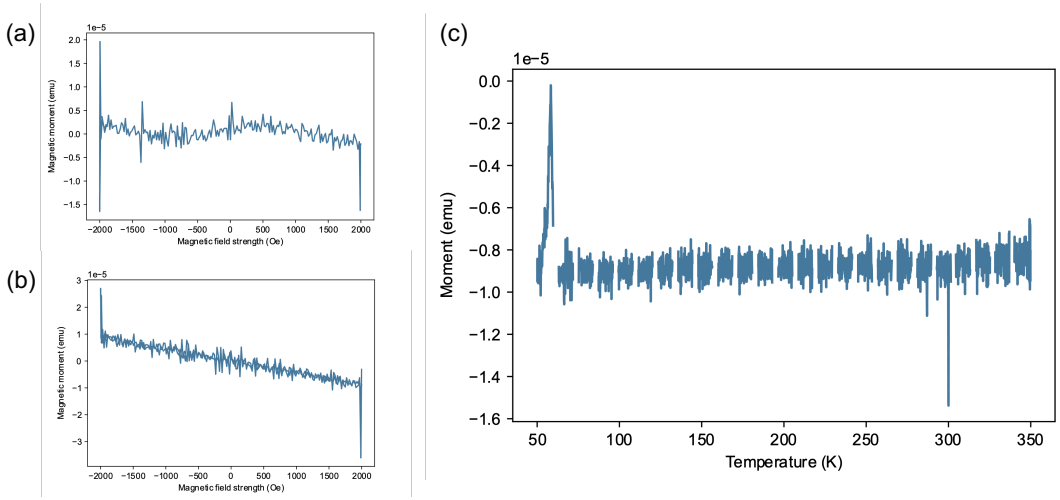

Figure 4.19: Measurements of the magnetic moments by VSM on sample T-2000 indicate no ferromagnetic ordering. Hysteresis measurements at 50 K for (a) as-deposited sample and (b) after additional annealing. (c) Magnetic moment with temperature.

coefficient is largest for low wavelengths, and decreases exponentially, converging towards zero as the wavelength increases. Approximating the decrease of k with a Tauc plot in its linear region, the absorption is thus highest for wavelengths in the range of 350-400 nm. This is ultraviolet light and corresponds to an approximated band gap energy in the range of 3.10-3.35 eV.

4.9 Vibrating-sample magnetometry

Control of growth modes is an important step towards control of the functional properties of the film. The magnetic properties of the thin film were measured with a vibrating-sample magnetometer. The aim was to measure the saturation magnetisation and the magnetic transition temperature, but hysteresis measurements at 50 K showed no ferromagnetic response and therefore no presence of ferromagnetic phases. Further, there was a large degree of noise in all measurements. As-deposited, the magnetic response of the sample was solely from the sample holder as seen in Figure 4.19a. Additional annealing caused a change in the magnetic response, where the induced magnetisation is opposite of the applied field as seen in Figure 4.19b. Following measurements of the temperature-dependence of the magnetic moment, presented in Figure 4.19c, showed no temperature dependence of the magnetisation. As for the hysteresis, a weak induced magnetic field is detected, directed opposite of the applied magnetic field.

Chapter 5

Discussion

Herein, the results presented in Chapter 4 are evaluated. First, an evaluation of the substrate preparation procedure is given. Next, the observed growth characteristics during pulsed laser deposition of thin film LNMO is discussed, focusing on the effect of substrate morphology, target-substrate distance and film thickness. A review is then given of the crystal structure. Finally, the magnetic and optical properties of the films are discussed.

5.1 Substrate preparation

This section evaluates how water purity and annealing parameters used during substrate preparation, influences the final structure of the surface. Moreover, the resulting surfaces are compared to those obtained by the standard preparation procedure based on BHF-etching.

5.1.1 Water purity during etching

Substrate preparation is performed to achieve atomically flat substrate surfaces for subsequent growth of epitaxial LNMO films. Selective Sr-etching was performed with different water qualities, and UP, DI and tap water all resulted in atomically flat terraces and increased structural ordering. UP water resulted in step edges with a lace-like structure, while DI water and tap water gave straight step edges. Overall, the structure from tap water and UP water was more disorganized, and the lace structure is expected to increase disorder, and thereby promote roughening during growth of films. The concentration of ions in tap water will differ depending on local variables in countries and labs, thus making it challenging to develop a standardized procedure based on this type of water [60].

A limitation of the study of the effect of water purity, is the use of only one sample for testing UP and tap water, providing low statistical significance. The three tested samples were however prepared in the same batch. The step-edge configuration observed

by UP-water etching was not observed for any substrates etched with DI-water. Hence, we interpret that the unique terrace termination of this sample originates from the lower content of ions in UP water compared to DI water [61]. Consequently, these observations confirm that DI-water is the preferred purity for water-etching of (111)-oriented STO due to the straight step edges, in agreement with the procedures used in literature [35–37]. Additionally, DI water offers a standardized ionic concentration.

5.1.2 Annealing parameters

The experimental series where annealing parameters were varied, show some trends in terms of the effect of annealing temperature and dwell time. Reduction of the annealing temperature from 1150°C to 1125°C, while the dwell time remained fixed at 2 hours, reduced the overall amount of step-bunching. However, the resulting surface showed combinations of droplet shapes and monolayer steps. Although reduction of the temperature reduced the amount of step-bunching, it also resulted in a less ordered structure. Comparable observations were made when the dwell time was reduced from 2 hours to 1 hour while the temperature was fixed at 1150°C, which reduced the amount of step bunching and gave a more uniform step-and-terrace structure with narrower terraces. Consequently, it indicates that step-bunching is induced by high-temperature annealing and that higher temperature or longer dwell time can promote step-bunching.

At 1125°C, an increase of the dwell time from 2 hours to 5 hours changed the step morphology from a combination of droplets and steps, to a faceted structure. For straight step edges, one crystal facet is primarily exposed, while a faceted step edge exposes a combination of facets with different energy. Then, long, high-temperature annealing has caused reconstruction of the surface where it is more energetically favorable to expose other crystal planes. The faceted step edge morphology that was achieved after annealing for 5 hours resembles the morphology that Hallsteinsen et al. [36] observed by DI water etching and annealing at 1200°C for 2 hours. For their substrates, the $(11\bar{2})$ and $(\bar{1}2\bar{1})$ crystal planes were exposed on step edges, similar to what is observed in this work, and the zigzag pattern on the step edge followed the crystallographic axes. However, the obtained surfaces of Hallsteinsen have a consistent step height of one monolayer. The observed steps in this work range from one to seven monolayers, with an average step height of three. Compared to the work of Hallesteinsen et al., where substrates were annealed at a higher temperature for a shorter time span, the same morphology is observed while it now includes slight step-bunching.

Differences in the shape of the step edges can originate from different chemical terminations of the terraces. It has been shown that simple thermal treatment of STO(001) above 1200°C causes a progressive enrichment of SrO on the surface, without increased surface roughness [39]. The transition is associated with a transition of the surface morphology from straight step edges during TiO_2 termination to faceted step edges during SrO termination. A similar transition mechanism may explain the observed faceting by long-

temperature annealing, and the mixed termination with areas of gradual height increase for intermediate annealing conditions. Confirmation of this hypothesis would require further LFM studies to characterize possible regions of deviating chemical termination.

Compared to the state-of-the-art preparation procedure by BHF etching and DI water etching, the obtained results from substrate preparation are less reproducible, and all procedures gave more step-bunched surfaces. Annealing parameters should be explored further, for instance by preparation of more substrates by annealing at 1150°C for 1 hour and by exploring the effect on the substrate by annealing at 1125°C for 1 hour. When the correct morphology is achieved in terms of step edge structure and step-bunching, reduction in the degree of mixed termination might be achieved by additional rinsing with DI water, as suggested by Hallsteinsen et al. [36].

From the preformed work with substrate preparation, it can not be concluded if the obtained surfaces are purely single terminated. All substrates are dominated by step heights that are integer multiples of d_{111}. However, half-integer multiples are also observed on most substrates, indicating mixed termination. The LFM characterization performed on one substrate give indications of single termination, but with frictional contrast close to faceted step edges. More LFM characterization, especially on substrates with a more apparent step-and-terrace structure, should thus be performed to confirm single termination in these cases.

Trends were identified in the effect of annealing time and temperature on the resulting surface morphology, but the trends were not definite. During the experimental work, the provider of substrates changed from SurfaceNet GmbH to Shinkosa. The providers use different techniques to obtain high-purity STO crystals. Hence the concentration of impurities may differ between substrates from the two providers. During the performance of experimental work, this was not regarded. Hence, the difference in substrate providers might explain the deviations in obtained morphology between substrates prepared by the same method. For future work, optimization should focus on substrates from one provider, as etching and reconstruction through annealing is highly sensitive to crystal purity.

In conclusion, the most well-defined step-and-terrace structure was observed on two of the substrates annealed at 1150°C for 1 hour. These were the best among the observed surfaces due to straight step edges and consistent step height in observed areas, with a quality comparable to that achieved by etching with BHF. Nevertheless, the substrate exhibited step heights that were integer and half-integer multiples of one monolayer, indicating a mixed termination.

5.2 Film growth

Here, the growth mode of the deposited LNMO films is assessed by evaluation of the AFM-characterized surface morphology of deposited films and the in-situ growth characterization through RHEED. The growth rate is estimated, and suggestions are given for further optimization of the growth process.

5.2.1 Effect of substrate surface morphology on film growth

Results of AFM characterization on films show that the substrate topography determines the surface topography of the grown films. The large degree of dependence, which indicates large interactions between film and substrate, is a control parameter for the film. Control of the substrate topography gives control of the surface morphology and the growth mode, and the substrate surface should thus be designed to promote the desired structure of the film.

It is prominent that the growth of the film largely depends on the morphology of the substrate surface. This is illustrated on the surface of T-2000, where increased roughening in areas with small terraces compared to large terraces suggests that the growth mode differs depending on the local environment on the terrace. Step edges are important nucleation sites for deposited ad-atoms [62], and can induce imperfections in the film by step-induced strain. When films have an out-of-plane lattice parameter that differs from the substrate, step-edges induce a shift in the stacking that proceeds as a dislocation through the film. It is therefore suggested that step-bunched substrates stabilizes layer-by-layer growth by providing wider terraces and reduced dislocation densities. In summary, it is not trivial to state if a step-bunched substrate with single termination, or a surface with mixed termination and many step edges, has the preferred morphology.

Ultimately, studies on surface roughness and growth mode of thin films would benefit from film growth on substrates with similar chemistry and morphology. This ensures a similar energetic environment for all deposited films, which is a prerequisite to study the effect of individual parameters on the growth mode. Thus, establishing protocols for substrate preparation is an important step toward enabling such studies.

5.2.2 Effect of target-substrate distance on the initial growth mode

Assessing the impact of target-substrate distance on the growth mode, the topography of all films replicated the topography of the substrate. The films grown with the longest distance, D-43 and D-46, showed simultaneous growth of multiple layers through a birth-and-spread mechanism. Indications of such a growth mechanism were not observed for D-35 and D-40, which appear to grow layer-by-layer with a slight smoothing of substrate irregularities. The degree of step-bunching varies between substrates, but is relatively sim-

ilar for D-35, D-40 and D-46. Thus, the observed surface structures can indeed indicate that smaller target-substrate distance suppresses 2D nucleation and growth of multi-layer planar sheets, and promotes layer-by-layer film growth during the initial growth period. This is in accordance with the observations from the fall semester, which motivated performance of this study [10].

For D-35 and D-46, the surface roughness on terraces decreased by film growth. Not only did the film not roughen the surface, but the roughness went down. This observation can be explained by incorporation of atoms that make up the slight roughness of the terrace into the first film layers. The STO surface can be reconstructed, while the surface of LNMO is more stable. Another aspect that should be considered, is that AFM is a local imaging technique, and the imaged areas on substrate and film are not exactly the same. The roughness will deviate across areas, and imaging of different areas will largely influence the roughness numbers. Additionally, the uncertainty of the numbers for roughness for both sample substrates, covers the average roughness of the films, and the observed decrease may be explained by the statistical distribution of roughness numbers.

To understand the effect on the growth of thicker films, closer to the thickness required for functional application, growth of thicker films would be interesting. Such an experiment would allow for observation of increased roughening and comparison of the surface roughening of several films with the same thickness. This work observed the effect of target-substrate distance for the first 500 laser pulses only.

RHEED enables study of the growth process of each individual monolayer and can supplement the AFM-observations of the growth mode. However, RHEED studies were not successfully performed during growth of these films, due to instabilities in the deposition system and ongoing optimization of the technique during the semester. If RHEED had been performed, it would allow for the study of the growth mechanism during deposition of the initial layers, possibly identifying differences in growth mechanisms between films. Thus, the indications from AFM can be confirmed or disproved.

The optimal target-substrate distance depends on the laser energy and the background pressure in the chamber [63], as the combination of these parameters determines the energy of ad-atoms during deposition. When the target-substrate distance is changed, other parameters must subsequently be adjusted for the energy of deposited ad-atoms to be the same. Based on the performed work, it is not possible to quantify how the laser energy and oxygen pressure should be adjusted. This is however mentioned because the parameters might be adjusted in later studies, to keep the ad-atom energy constant while changing the target-substrate distance, which is favourable to reduce the time spent for each deposition.

In conclusion, the results of this work show that the sensitivity of the growth mode to target-substrate distance within the explored 35-46 mm range is small, with an indication that shorter distance is preferential due to prolonged layer-by-layer growth.

5.2.3 Growth evolution evaluated by AFM

In the study of surface roughening with film thickness, a gradual roughening of the surface was observed. A transition from layer-by-layer growth was identified in the growth region between 500 and 1500 pulses. After the onset of roughening, the surface goes rougher as the film grows. This observation is in accordance with the layer-island growth mechanism, where the growth mode changes to island growth for strain relaxation. Additionally, it was observed that the growth mode depends on the substrate morphology, and that smaller terraces lead to an earlier onset of rough growth. Similarly, wider atomically flat terraces, as found on T-500 and T-1500, do not roughen as quickly as narrower terraces. This effect prolonged the critical thickness before the growth mode changed from layer-by-layer to island growth.

Chakraverty et al. observed that the surface of perovskite $SrFeO_{2.5}$ grown on STO(111) was rough with triangular islands, compared to (001)-oriented films that maintained the original atomically flat surface structure of the substrate [64]. They stated disordered atomic structures at heterointerfaces as a possible explanation for this difference. In comparison, the films grown in the work of this thesis are not as rough. However, the film thickness in the work of Chakraverty et al. was 75-260 nm, while the films deposited in this work are all below 75 nm. The RHEED pattern is similar with a signal dampening after 100-200 seconds, thus the initial growth appears to be the same.

The effect of surface morphology becomes especially important in this growth series. Here, sample T-1500 illustrates the prolonged layer-by-layer growth on wider terraces. It demonstrates that the critical thickness of the film depends on the substrate surface, and that wider terraces appear to prolong the thickness for which growth happens layer-by-layer. Growth on more similar substrates, with the same terrace width, -termination, and step edge shape, would improve information on the critical thickness and transition of the growth mode for a given substrate structure. Accordingly, the obtained results can not be used to give a precise critical thickness. Rather, it demonstrates a gradual roughening and a transitioning growth mode from layer-by-layer to island growth as the film grows thicker.

Roughness variations across sample

Generally, the roughness of the surface was different between the areas that were imaged. The variation in roughness across the sample surfaces was especially prominent during the inspection of sample T-4000, where the structure of the surface was prominently different between the inspected areas (Figure 4.7). This film was grown on a 10×10 µm^2 large substrate, and inspected areas were located far away from each other. During pulsed laser deposition, the plasma plume that transfers ad-atoms to the surface is highly forward-directed. Accordingly, the energy of ad-atoms in the center of the plume will be larger than the energy of the atoms that are further out [42]. When the ad-atoms land on the

substrate surface, the energy will also be different depending on where in the plume the atoms have traveled, and can give growth in different growth modes [65]. Plasma plume dynamics is a complicated field of study that has not been regarded in the work of this thesis. However, the result indicated that the 10×10 µm^2 substrate is large enough for the variations in the plume to have a considerable effect on the growth mode. The effect of this mechanism was not evaluated in detail for the other samples, although all films had some degree of variation across inspected areas. However, it is reasonable that the effect is most prominent for sample T-4000, which is the thickest sample.

5.2.4 Growth mode evaluated by RHEED

Diffraction pattern

During deposition, the diffraction pattern changes from a semi-circle to a rectangular pattern. This shift means that the surface roughens through growth, and is in accordance with the growth mode observed from AFM surface inspection and RHEED intensity tracking.

During deposition, the intensity of the diffraction pattern always disappeared rapidly. As seen in Figure 4.9, the diffraction pattern produced by the surface of sample X-1 was weak at the incident angle, where it was optimized for diffraction from the STO substrate, and more defined when the sample was rotated by 30°. It indicates that the optimal orientation of the sample for diffraction is different between substrate and thin film crystal, and can indicate that the pseudo-cubic unit cell of LNMO is oriented differently from the cubic unit cell of STO and not placed perfectly on top. For future growth tracking with RHEED, the system could therefore benefit from alignment to the other 30° symmetry line of STO, illustrated in Figure 2.4b, as this appears to be the preferred orientation to observe the diffraction from the LNMO crystal.

Intensity tracking

The intensity of the RHEED pattern dampens quickly after the onset of deposition. Similar rapid loss of signal is observed in [64] for PLD deposition on STO(111). Chakraverty et al. relate the rapid dampening to the unstable nature of the surface, which they describe quickly makes the growth transition to a rougher growth mode [64]. The rapid loss of intensity of the RHEED diffraction spots is thus because the surface is three-dimensional, following roughening. Amorphous growth of the film could also describe the loss of the diffraction signal, which requires a crystalline sample surface. However, TEM imaging of sample T-1500 contradicts this theory, as the sample is found to be highly crystalline. It can also be described by relaxation of the growth parameters or domain formation, that is difficult to identify from the present TEM images. Therefore, we relate the signal loss to a roughening of the surface after the growth of the first monolayers.

The RHEED signal in Figure 4.12 confirm layer-by-layer growth for the first monolayers. Additionally, the two first oscillation pulses appear in a pair, where the minimum is only halfway from the minima in the past pulse. The origin of this is unknown. If we assume that each layer has a linear increase in roughness, a suggeste explanation is that two complete perovskites layers are more ordered than one single layer. Another possibility is that the LNMO/LNMO interface is more stable than the LNMO/STO interface. Similar oscillation patterns were observed by Gunkel et al., that observed appearance of secondary RHEED oscillations which dampen over time when the growth of A-site double perovskite praseodymium barium cobalt oxide transitioned from growth of a common perovskite structure, to an oxygen-vacant ordered quasi double perovskite structure, following temperature elevation [66]. The additional oscillations resemble those observed in Fig 4.12. Yet, the number of oscillations in Figure 4.12 is much fewer (only 5), not enough to observe if the secondary oscillations gradually dampen as observed in the work of Gunkel. Nevertheless, it indicates that if growth and RHEED signal is stabilized over longer time, RHEED can provide information about the ordering of double perovskite structure. However, one RHEED intensity oscillation should correspond to the completion of the double perovskite unit cell, because all deposits must be consumed to reach the oscillation maximum [42]. Thus, completion of individual layers containing B-site cation Ni or Mn alone should not result in a separate oscillation [67], although it could change the intensity of the maximum or minimum points to give a kind of superstructure in the pattern. The ordering direction for the system of Gunkel was the [001]-direction rather than the [111]-direction, which can explain their observed additional oscillations.

RHEED studies were also performed in the lab last semester [10]. Then, the period of intensity oscillations varied between 7 and 9 laser pulses. In comparison, the one film that was grown with successfully RHEED tracking during the work of this master thesis, had intensity oscillation periods between 12 and 14 pulses. As the deposition chamber, the target material and the deposition parameters are the same, the observed change in oscillation period was not expected. A possible explanation is that the oscillations observed last semester came from the RHEED instabilities that was identified in this work. Specifically, instabilities were introduced from pressure variations and target rotation, as described in section 4.4.3. Limiting these effects, through fixation of the throttle valve and reduction of the target rotation speed, made it possible to identify the layer-by-layer oscillations. The period corresponds well with the expected growth rate of one monolayer, and we therefore propose that the oscillations are real and originate from film growth.

5.2.5 Measurements of film thickness

The film thickness was estimated by TEM, ellipsometry and RHEED. Direct measurement from cross-sectional TEM imaging measured a thickness of 23 nm on sample T-1500. In comparison, indirect estimates through ellipsometry gave a thickness of 24 ± 0.545 nm for the Cauchy Extended model on T-2000 and 66.86 ± 0.424 nm for the Graded Layer model on T-4000. For growth by 1500 pulses, this corresponds to 18.0 nm and 25.1 nm, respectively, thus the Graded Layer model on T-4000 fits well with the measurement from TEM. Note that the surface of T-4000 is considerably rougher than the thinner T-1500 and T-2000 samples, with height deviations up to 4 nm.

The TEM thickness is directly measured from electron microscopy images, and the uncertainty is generally only a few nanometers. However, uncertainty is introduced to this method because of the non-optimized preparation method, where the ion beam can ruin the surface, and the surface roughness can be masked by the carbon top coating. This can introduce local variations in the thickness of the TEM sample.

In contrast, the estimates from ellipsometry are found through indirect measurements based on reflection, and use a model fitting with several degrees of freedom. For ellipsometry, the model is regarded as a "good fit" if the mean-square error between the measured data and the fitted model is below 10, while the MSE is between 20 and 40 for the utilized models. Although the fit is not ideal, the quality is acceptable to give thickness estimates but has a significant uncertainty that exceeds the uncertainty stated by the model, as seen in the numbers given above. The uncertainty is also higher for this method, as it is used to characterize thicker films with surface roughness up to several nanometers.

In RHEED, the observed layer-by-layer oscillations during the growth of sample X-1, correspond to a thickness of 25.8 nm after 1500 s of growth. Again, the uncertainty is of a few nanometers due to the unknown d-spacing, and measuring error during measurement of the oscillation frequency. It should also be noted that the growth rate can change as the growth mode proceeds to island growth, although the deposition rate is constant.

To conclude, the utilized techniques for thickness characterization indicate a film thickness of ≈ 25 nm for films grown by 1500 laser pulses. This thickness corresponds to a growth rate of ≈ 0.1667 Å/s. These numbers are associated with uncertainty, as a small number of samples have been characterized by each technique. Perhaps even more important, improved numbers require optimization of the utilized techniques for the material system. More specifically, improvement of the sample preparation procedure for preparation of cross-section TEM-lamellas, ellipsometry on more films to create a more precise model for the optical constants, and confirmed stabilization of the RHEED system, is required. Unfortunately, such optimization was past the scope of this thesis, and the results should be regarded as preliminary estimates.

In thin film studies, the ability to measure the film thickness by robust, easy, quick and non-destructive methods is important to understand the structure of deposited films. These capabilities are offered by ellipsometry and x-ray reflectivity (XRR). However, a weakness with ellipsometry is that it is an indirect measurement technique based on model fitting. During this work, the models were not adequately fit to the optical constants of STO and LNMO, which is required for high-quality estimates. On the other hand, XRR and XRD provide direct measurements of the thickness with the similar advantage of being non-destructive, without the requirement of finding model parameters. X-ray-based thickness measurements were, however, not successfully performed in the work of this thesis, and the performed measurements showed no thickness fringes. Lack of thickness fringes in XRD can be because of poor sample quality, as dislocations, local point defects, interface or surface roughness blurs the fringe pattern [68]. For XRR, the signal might have been reduced because of interface roughness, poor density contrast between substrate and film, or poor alignment of the sample and XRD system [69].

5.2.6 Effect of glue on substrate temperature and growth mode

Proper RHEED intensity tracking was only achieved during deposition of the last film, sample X-1. Although instabilities in the electron beam due to the discussed fluctuations in the chamber caused reduced electron beam signals during prior deposition, there is one other possible explanation for the rapid dampening of the specular spot intensity. During deposition of most films (all except T-4000 and X-1), epoxy glue was used to fixate the substrate to the substrate holder due to a misunderstanding of the procedure. The substrate is heated during deposition to provide energy for ad-atom diffusion. A heating element heats the substrate holder, which the substrate is fixed to with this glue. Normally, silver paste is used for gluing due to its thermal conductivity, which ensures sufficient heat conduction to the substrate and surface atoms. In contrast, the epoxy glue has much lower constants for thermal conduction [70, 71]. Lack of thermal transfer reduces the surface energy on the substrate, lowering the actual substrate temperature during deposition and, subsequently, the kinetic energy of ad-atoms. The reduction in kinetic energy of ad-atoms can cause amorphous or less crystalline growth, or faster transition to island growth, observed as a rapid change of the diffraction signal from bright diffraction spots to a blurry shadow from the randomly scattered electron beam. Amorphous surfaces are expected to create a continuous semi-circle diffraction pattern rather than a blurry shadow, so the information from diffraction patterns is inconclusive [72], but indicate a rapid transition to a rougher surface. TEM characterization of sample T-1500, deposited with epoxy glue, showed that the sample was crystalline. Therefore, the growth process is not amorphous. However, the lowering in deposition temperature could reduce the crystal quality and change the growth mode. For future studies, it is therefore advised to use silver glue for sample fixation for increased control of the substrate surface temperature.

Control of the growth temperature is important, as it influences the crystal quality and growth mode. Additionally, it influences the degree of B-site ordering in grown double-

perovskites. Singh et al. compared growth of LNMO at 500°C and 800°C, and identified that Ni/Mn-ions ordered during high-temperature deposition [22]. Even though there was a difference in the crystal structure, they identified epitaxial, crystalline LNMO for both deposition temperatures. In the work of this thesis, the deposition temperature was set to 500°C. This was chosen because of the unstable nature of (111) substrates, where lower deposition temperature has been found to stabilize the growth process of perovskites [73]. Nevertheless, further, uncontrolled reduction of the temperature through poor thermal conductivity from substrate heater to substrate can have caused unexpected changes in both deposition temperature and growth mode.

5.2.7 Summary of key findings

In summary, control of the film surface is achieved during growth of LNMO thin films on (111)-oriented STO substrates. Variations in surface roughness indicates that shorter target-substrate prolongs layer-by-layer growth. The growth mode changes from layer-by-layer growth to island growth after a critical thickness, that is found to depend on the structure of the substrate surface, which give rise to surface roughening. The growth rate is estimated to 0.1667 Å/s. For further optimization of the growth process, it is suggested that films are grown on substrates with the same structure to enhance comparability. Additionally, RHEED can possibly be optimized by aligning the electron beam to the other symmetry direction of the crystal, and silver paste glue should be used to fixate the substrate to increase the control of deposition temperature.

5.3 Measurements of crystallinity

This section reviews the characterization methods that have been used to identify the crystal structure of the prepared thin film samples. TEM characterization of a cross-section confirmed that the film was crystalline. The observation was supported by XRD, lacking amorphous or polycrystalline observations while suggesting epitaxy. However, neither XRD nor Raman provided the expected precise information on strain and symmetry group due to shadowing from the substrate.

5.3.1 TEM

The high-resolution TEM images confirm that the inspected film is crystalline and without grain boundaries in the inspected areas. The film appear to be fully epitaxial, although more accurate measurements are needed to tell so for certain. However, the crystalline quality of the TEM cross-sectional sample was not good enough to perform electron energy loss spectroscopy (EELS), to fully confirm short-range order or identify the valence state of the transition metal oxides, which is relevant for both the crystal structure and the magnetic state [20]. The TEM sample preparation method was not good enough, which led

to bending of the sample and distorted the crystal structure, with subsequent appearance of amorphous domains [74, 75]. Even though TEM-imaging was only performed on one sample, it confirms that the deposition parameters produce crystalline films with a sharp interface between substrate and film.

5.3.2 XRD

The performed XRD scans support that the grown LNMO films are crystalline and indicate that the film is epitaxial on the substrate. Specifically, this is seen through the distinct diffraction peaks of the film on the detector scan around the (111) peak, corresponding to the expected alignment of the film on the substrate, supported by the width of the rocking curve, which is $< 0.2°$ [68]. Additionally, the film peak is observed on the right-hand side of the substrate peak, which is expected for epitaxial growth of LNMO on STO [50, 76]. Ultimately, it would be beneficial to collect reciprocal space maps that use multiple scans to observe the substrate and film peaks. This would provide more precise information about the strain and crystallography of the films and contribute to increased understanding of the asymmetrical peaks.

Next, the $\theta-2\theta$-scan, presented in Figure 4.13, displays weakly visible additional diffraction peaks. Similar observations were done by Singh et al., who detected four additional peaks around the STO(111)-peak, for a $\theta-2\theta$ scan from 15° to 65° on a Ni/Mn-ordered thin film [22]. They stated two possible explanations for these reflections. The first is that the film had a monoclinic symmetry with several domain orientations that are stable on STO(111) by a subtle relative change in the lattice distortions. The next proposed explanation for the additional peaks, is presence of superlattice reflections, observed as symmetric satellite peaks around the (111) and (222) peaks. These superlattice reflections originate from additional Ni/Mn ordering [77]. Only one peak in the broad $\theta - 2\theta$ scan performed during the work of this thesis overlaps with the scan that Singh performed, and it is located at 44° compared to 46°. Thus, it has not been possible to make a direct comparison of the structures. Broader scans around the (111) and (222) peaks would provide additional information and, if symmetrical, could be used to identify Ni/Mn ordering. The additional peaks in proximity to $2\theta = 66°$ and $2\theta = 77°$ may be identified as monoclinic (400) and (402) peaks originating from distortions in the orientation of the LNMO unit cell.

As the lattice constant of LNMO and STO is very similar, the film and substrate peaks overlap, making it hard to distinguish the film from the substrate. Something is seen from XRD, but not enough to determine the crystal structure or the amount of B-site cation ordering. Super-symmetry peaks from cation ordering are not observed either. In order to optimize scans, it might be helpful to characterize thicker films. Additionally, using a substrate with a more significant lattice mismatch, like LSAT, would make it easier to separate diffraction peaks belonging to the film from those belonging to the substrate.

5.3.3 Raman spectroscopy

Polarized Raman spectroscopy did not provide any information about the crystal structure of the characterized thin films. In fact, the obtained Raman spectra only show peaks that originate from the STO substrate, which is known to produce a strong Raman signal [78]. The strong Raman background signal of STO is known to hinder Raman studies on thin film growth on this particular substrate [79] since Raman spectra of both the film and the substrate are detected in the given experimental setup with such ultra-thin films. Thus, thin film characterization by Raman requires the possibility to separate the Raman spectra of the film from that of the substrate. To achieve such separation, the film should be grown on a substrate without Raman excitations that mask those from the film. For Raman studies of LNMO thin films, LSAT and LAO would be better substrates than STO, as they are not associated with these challenges [79].

5.4 Magnetic properties

VSM measurements of the magnetic properties of sample T-2000 displayed no ferromagnetic signal from the as-deposited film. A transition to diamagnetic behavior was observed following additional post-deposition annealing at 700°C in an oxygen atmosphere. After the first VSM measurement, when it was observed that the film was non-magnetic, it was assumed that the films were non-stoichiometric, specifically with a deficiency of oxygen atoms. Thus, additional annealing in oxygen was performed in an attempt to introduce more oxygen into the material, as the magnetic properties of LNMO originates from Ni^{2+}-O-Mn^{4+} exchange interactions that will be suppressed by the appearance of secondary phases, locally disordered Ni and Mn ions, and oxygen deficiencies [49, 53].

Kitamura et al. grew LNMO thin films on (100)-oriented STO by pulsed laser depositon and found that the parameter window of optimized conditions for ferromagnetism was very narrow [53]. In their work, ferromagnetic phases were only achieved when the oxygen pressure was above 0.5 mbar, which is several orders of magnitude larger than the pressure used during growth in this work. Similarly, optimized conditions required a growth temperature of 700°C, compared to the set point temperature of 500°C used in the work of this project. Although the work of Kitamura was done on (100)-oriented films, this indicates that an increase in deposition temperature or ambient pressure might be required to obtain a ferromagnetic phase in the deposited LNMO thin films. Unfortunately, this has not been possible for the work of this thesis, as a component of the utilized deposition system, the heater shield, degrades when exposed to high temperatures and high oxygen pressures. However, the performed experiments show that post-deposition annealing changes the degree of magnetic ordering, thus this can be explored further as a solution to improve the stoichiometry and magnetic properties. Additionally, an increase in the deposition temperature from 500 to 700°C has been found to make the growth process of films in the [111]-direction less stable, which reduces the critical thickness before island

formation [32]. Therefore, the reduction of oxygen vacancies by post-growth annealing rather than elevated growth temperatures is suggested as an approach that can improve stoichiometry and maintain the layer-by-layer growth mechanism.

Unless highly surface sensitive, characterization methods used to study the properties of thin films measure signals from both the substrate and the film. This is also the case for VSM, which measures the magnetic response from both LNMO film and the STO substrate. STO has an intrinsic diamagnetism [80]. Usually, this contribution is subtracted during analysis to identify the contribution from the thin film on the magnetic signal [32]. The diamagnetism from the substrate might explain the measured diamagnetism after annealing. However, the question of why this is not measured before annealing remains, as the annealing procedure should not alter the magnetic properties of the substrate. Nevertheless, the results indicate that post-growth annealing induces a change in the sample's magnetic properties, whether in the LNMO thin film, the substrate, or glue residue on the substrate. Unfortunately, the VSM machine was shut down following the acquisition of this data, hence the source of the magnetic response change was not investigated further. Repeated measurements, and characterization on more samples, can be performed to identify the source of the diamagnetic response. Suggestions for work include annealing of more samples to see if the same change in magnetic behavior is observed, measurements on STO substrates alone, and further investigation of the magnetic properties of the epoxy glue that had left residues on the back-side of the substrate.

However, the key takeaway from the VSM measurements is that the growth parameters used in this work produced non-ferromagnetic LNMO thin films. Further optimization of growth parameters is needed to obtain correct stoichiometry in the films, which is required for the ferromagnetic and photoferroelectric properties that is aimed for when LNMO is grown for photovoltaic applications.

5.5 Optical properties

Ellipsometry estimated the refractive index and extinction coefficient as a function of wavelength through a Cauchy Extended model. The results from ellipsometry characterization showed an increase in the refractive index and a shift of its maximum value towards longer wavelengths, following a increase of the film thickness between sample T-2000 and sample T-4000. It is observed that only ultraviolet light is absorbed and that the absorption decreases for longer wavelengths, in agreement with the observed slight yellow color of the deposited thin films. Thus, the material is a poor absorber of most of the visible spectra. The band gap estimate of 3.10-3.35 eV is far higher than the optimal 1.1 eV band gap, that makes LNMO interesting for IBSC applications. Previous studies have shown that LNMO thin films can absorb light from the ultra-violet, visible, and half of the near-infrared region of the solar spectrum [81], thus the potential for absorption is larger than what is achieved for the investigated samples. Hence, the deposition parameters must be

adjusted, and more work must be performed for the band gap of LNMO to obtain the requested value.

A critique of the used method is that the Cauchy Extended model is a poor model for band gap measurements. For improved estimates and band gap measurements, the use of higher-quality oscillator models, better suited for oxides, is suggested [82, 83]. Additionally, more samples should be characterized to improve the models and increase understanding of ellipsometry data collected from the material system.

Chapter 6

Further Work

Herein, suggestions for further improvement of the procedures for pulsed laser growth of (111)-oriented LNMO thin films are given.

The surface of the substrate a thin film is grown on, was seen to have a sizable effect on the growth process, particularly the critical thickness. The surface preparation procedure with DI water would therefore benefit from further optimization and confirmation of the reproducibility, focusing on substrates from one provider. More specifically, exploration of annealing parameters around the 1500°C for 1 hour procedure is suggested, like 1125°C and 1175°C for 1 hour. LFM studies should be performed to increase the understanding of the polarity of the surface. If mixed termination is identified, the effect of an additional water rinse on the termination can be assessed.

To increase the understanding of growth of LNMO thin films, the critical thickness should be identified by comparing films grown on substrates with a more similar surface structure. This will make it easier to identify how different deposition parameters influence the growth process, particularly the critical thickness, in later growth studies.

Future studies will benefit from methods for characterization of the crystalline quality, epitaxy, and cation ordering, beyond those utilized in this project. Further characterization of the crystal structure and epitaxy through XRD is suggested. Herein, analysis of the observed additional diffraction peaks is of particular interest. Films grown during this work have been sent to a synchrotron facility for 2D mapping of the reciprocal space, to investigate the additional peaks and separate the film peaks from substrate peaks. Hopefully, this will contribute to an increased understanding of the structure of the films.

Another suggestion is to grow LNMO thin films on LSAT(111) substrates. Because the substrate does not have the reported problems of overlapping diffraction peaks and Raman-signals during characterization, this can ease the characterization of the film's crystal structure. As for growth on STO, growth on LSAT has been found to promote B-site cation ordering [50].

Improvement of the characterization methods for functional properties is also suggested. Specifically, the model used for band gap measurements in ellipsometry should be advanced using oscillator-based models and larger sample sets. Other methods, like photoemission spectroscopy, can also be used to measure the band gap.

In order to confirm that the lack of ferromagnetic phases arises from stoichiometry deviations in the films, EELS measurements of cross-sectional samples is suggested. EELS can be used to map the content of elements in the sample, thereby quantifying the ordering of ions in the structure. Ultimately, it can provide an improved understanding of stoichiometric challenges.

To improve the stoichiometry of the films and enhance the chances of accomplishing the functional properties that are desired for application in intermediate band solar cells, it is prominent that deposition parameters must be adjusted. In particular, the oxygen pressure during deposition should be increased to enhance the oxygen content, which is indispensable for magnetic exchange interactions. This adjustment might require subsequent changes in the laser energy or target-substrate distance to maintain a stable growth process. Further iterations of the growth parameters are required to increase the understanding of intermediate band formation in double perovskites.

Chapter 7

Conclusion

In double perovskites, several band gaps can be introduced to advance the performance as solar absorbers, producing intermediate band solar cells. A prerequisite is precise control of the growth process of the material. By analyzing the surface morphology, crystal quality, magnetic and optical properties of LNMO thin films grown on STO in the [111]-direction, this master thesis has shown that such control can be achieved through pulsed laser deposition.

The surface structure of films was found to replicate that of the substrates they were grown on. Ordered substrate surfaces, that promoted high-quality growth, were achieved by preparation with DI water and subsequent annealing at 1150°C for 1 hour. The preparation method yielded ordered substrate surfaces with satisfactory quality for further thin film growth, using a safe, simple, and environmentally friendly method.

The target-substrate distance during PLD growth seemingly has a minor impact on the initial growth mode, although results indicate that shorter distance prolongs layer-by-layer growth. Additionally, it has been shown that the surface of films becomes rougher with increasing film thickness, due to a transition of the growth mode from layer-by-layer to island growth. Step bunched substrates, and subsequent wider atomically flat substrate areas, is found to stabilize the growth mode and increase the critical thickness.

It was shown that further optimization of the growth parameters is required to obtain the desired functional properties, specifically ferromagnetism, photoferroelectricity, and a 1.1 eV band gap. Although TEM characterization confirmed growth of crystalline films with a sharp interface to the substrate, VSM measurements of the magnetic moment showed that the inspected film was non-magnetic. Hence, the stoichiometry and cation ordering that was aimed for, was not achieved.

To conclude, control of the surface morphology of LNMO grown on STO(111) by PLD has been obtained. Further work is required to optimize the deposition parameters for synthesis of stoichiometric, cation-ordered double perovskite thin films with the functional properties requested for solar applications.

Bibliography

[1]P. Forster, T. Storelvmo, K. Armour, W. Collins, J.-L. Dufresne, D. Frame, D. J. Lunt, T. Mauritsen, M. D. Palmer, M. Watanabe, M. Wild and H. Zhang, 'The Earths Energy Budget, Climate Feedbacks, and Climate Sensitivity. In Climate Change 2021: The Physical Science Basis. Contribution of Working Group I to the Sixth Assessment Report of the Intergovernmental Panel on Climate Change'.

[2]S. Rühle, 'Tabulated values of the ShockleyQueisser limit for single junction solar cells', Solar Energy **130**, 139–147 (2016).

[3]M. Kumar, A. Raj, A. Kumar and A. Anshul, 'Theoretical evidence of high power conversion efficiency in double perovskite solar cell device', Optical Materials **111**, 110565 (2021).

[4]M. A. Green, E. D. Dunlop, J. HohlEbinger, M. Yoshita, N. Kopidakis and X. Hao, 'Solar cell efficiency tables (Version 58)', Progress in Photovoltaics: Research and Applications **29**, 657–667 (2021).

[5]M. A. Green, A. Ho-Baillie and H. J. Snaith, 'The emergence of perovskite solar cells', Nature Photonics **8**, 506–514 (2014).

[6]M. Sariful Sheikh, D. Ghosh, A. Dutta, S. Bhattacharyya and T. Sinha, 'Lead free double perovskite oxides Ln 2 NiMnO 6 (Ln = La, Eu, Dy, Lu), a new promising material for photovoltaic application', Materials Science and Engineering: B **226**, 10–17 (2017).

[7]A. Hossain, A. K. M. Atique Ullah, P. Sarathi Guin and S. Roy, 'An overview of La2NiMnO6 double perovskites: synthesis, structure, properties, and applications', Journal of Sol-Gel Science and Technology **93**, 479–494 (2020).

[8]L. Jiang, I. Grinberg, F. Wang, S. M. Young, P. K. Davies and A. M. Rappe, 'Semiconducting ferroelectric perovskites with intermediate bands via B-site Bi5+ doping', Physical Review B **90**, 075153 (2014).

[9]M. Özcan, A. Allahbeickaraghi and M. Dündar, 'Possible hazardous effects of hydrofluoric acid and recommendations for treatment approach: a review', Clinical Oral Investigations **16**, 15–23 (2012).

[10]L. S. Joseph, *Pulsed laser deposition of double perovskite thin films on (111)-oriented SrTiO3 for solar cell applications*, tech. rep. (Norwegian Universtiy of Science and Technology, Trondheim, 2022).

[11]J. Nelson, *The Physics of Solar Cells*, 1st ed. (Imperial College Press, London, 2003), pp. 236–237.

[12]A. Luque, A. Martí and C. Stanley, 'Understanding intermediate-band solar cells', Nature Photonics **6**, 146–152 (2012).

[13]Z. Xiao, Y. Zhou, H. Hosono, T. Kamiya and N. P. Padture, 'Bandgap Optimization of Perovskite Semiconductors for Photovoltaic Applications', Chemistry A European Journal **24**, 2305–2316 (2018).

[14]Q. Sun, J. Wang, W.-J. Yin and Y. Yan, 'Bandgap Engineering of Stable LeadFree Oxide Double Perovskites for Photovoltaics', Advanced Materials **30**, 1705901 (2018).

[15]H. Li, F. Li, Z. Shen, S.-T. Han, J. Chen, C. Dong, C. Chen, Y. Zhou and M. Wang, 'Photoferroelectric perovskite solar cells: Principles, advances and insights', Nano Today **37**, 101062 (2021).

[16]K. Yi, Q. Tang, Z. Wu and X. Zhu, 'Unraveling the Structural, Dielectric, Magnetic, and Optical Characteristics of Nanostructured La2NiMnO6 Double Perovskites', Nanomaterials **12**, 979 (2022).

[17]R. Nechache, C. Harnagea, S. Li, L. Cardenas, W. Huang, J. Chakrabartty and F. Rosei, 'Bandgap tuning of multiferroic oxide solar cells', Nature Photonics **9**, 61–67 (2015).

[18]C. Tablero, 'Photovoltaic application of the multiferroic Bi2FeCrO6 double perovskite', Solar Energy **137**, 173–178 (2016).

[19]S. Vasala and M. Karppinen, 'A2BBO6 perovskites: A review', Progress in Solid State Chemistry **43**, 1–36 (2015).

[20]P. Ksoll, C. Meyer, L. Schüler, V. Roddatis and V. Moshnyaga, 'B-Site Cation Ordering in Films, Superlattices, and Layer-by-Layer-Grown Double Perovskites', Crystals **11**, 734 (2021).

[21]H. Guo, A. Gupta, M. Varela, S. Pennycook and J. Zhang, 'Local valence and magnetic characteristics of La2NiMnO6', Physical Review B **79**, 172402 (2009).

[22]M. P. Singh, K. D. Truong, S. Jandl and P. Fournier, 'Long-range Ni/Mn structural order in epitaxial double perovskite La2NiMnO6 thin films', Physical Review B **79**, 224421 (2009).

[23]N. S. Rogado, J. Li, A. W. Sleight and M. A. Subramanian, 'Magnetocapacitance and Magnetoresistance Near Room Temperature in a Ferromagnetic Semiconductor: La2NiMnO6', Advanced Materials **17**, 2225–2227 (2005).

[24]J. Blasco, M. Sánchez, J. Pérez-Cacho, J. Garca, G. Subas and J. Campo, 'Synthesis and structural study of LaNi1xMnxO3+δ perovskites', Journal of Physics and Chemistry of Solids **63**, 781–792 (2002).

[25]The Materials Project, 'Materials Data on SrTiO3 by Materials Project', `https://materialsproject.org/materials/mp-5229/`, *14/05/2022*, `10.17188/1263154`.

[26]H.-U. Habermeier, 'Thin films of perovskite-type complex oxides', Materials Today **10**, 34–43 (2007).

[27]M. Hashisaka, D. Kan, A. Masuno, M. Takano, Y. Shimakawa, T. Terashima and K. Mibu, 'Epitaxial growth of ferromagnetic La2NiMnO6 with ordered double-perovskite structure', Applied Physics Letters **89**, 032504 (2006).

[28]R. Ramesh and N. A. Spaldin, 'Multiferroics: progress and prospects in thin films', Nature Materials **6**, 21–29 (2007).

[29]J. Mannhart and D. G. Schlom, 'Oxide InterfacesAn Opportunity for Electronics', Science **327**, 1607–1611 (2010).

[30]N. Nakagawa, H. Y. Hwang and D. A. Muller, 'Why some interfaces cannot be sharp', Nature Materials **5**, 204–209 (2006).

[31]K. Momma and F. Izumi, 'VESTA3 for three-dimensional visualization of crystal, volumetric and morphology data', Journal of Applied Crystallography **44**, 1272–1276 (2011).

[32]I. G. Hallsteinsen, *Toward Growth Control of (111)-oriented Perovskite Thin Films: La0.7Sr0.3MnO3 / SrTiO3(111) a model study*, tech. rep. (Norwegian University of Science and Technology, Trondheim, 2012).

[33]J. L. Blok, X. Wan, G. Koster, D. H. A. Blank and G. Rijnders, 'Epitaxial oxide growth on polar (111) surfaces', Applied Physics Letters **99**, 151917 (2011).

[34]T. Ohnishi, K. Shibuya, M. Lippmaa, D. Kobayashi, H. Kumigashira, M. Oshima and H. Koinuma, 'Preparation of thermally stable TiO2-terminated SrTiO3(100) substrate surfaces', Applied Physics Letters **85**, 272–274 (2004).

[35]J. G. Connell, B. J. Isaac, G. B. Ekanayake, D. R. Strachan and S. S. A. Seo, 'Preparation of atomically flat SrTiO3 surfaces using a deionized-water leaching and thermal annealing procedure', Applied Physics Letters **101**, 251607 (2012).

[36]I. Hallsteinsen, M. Nord, T. Bolstad, P.-E. Vullum, J. E. Boschker, P. Longo, R. Takahashi, R. Holmestad, M. Lippmaa and T. Tybell, 'Effect of Polar (111)-Oriented SrTiO3 on Initial Perovskite Growth', Crystal Growth & Design **16**, 2357–2362 (2016).

[37]J. Chang, Y.-S. Park and S.-K. Kim, 'Atomically flat single-terminated SrTiO3 (111) surface', Applied Physics Letters **92**, 152910 (2008).

[38]A. Pojani, F. Finocchi and C. Noguera, 'Polarity on the SrTiO3 (111) and (110) surfaces', Surface Science **442**, 179–198 (1999).

[39]R. Bachelet, F. Sánchez, F. J. Palomares, C. Ocal and J. Fontcuberta, 'Atomically flat SrO-terminated SrTiO3(001) substrate', Applied Physics Letters **95**, 141915 (2009).

[40]G. Cao and Y. Wang, *Nanostructures and Nanomaterials*, Vol. 2 (WORLD SCIENTIFIC, Jan. 2011).

[41]L. Martin, Y.-H. Chu and R. Ramesh, 'Advances in the growth and characterization of magnetic, ferroelectric, and multiferroic oxide thin films', Materials Science and Engineering: R: Reports **68**, 89–133 (2010).

[42]R. Eason, ed., *Pulsed Laser Deposition of Thin Films* (John Wiley & Sons, Inc., Hoboken, NJ, USA, Nov. 2006).

[43]A. Fluri, C. Schneider and D. Pergolesi, 'In situ stress measurements of metal oxide thin films', in *Metal oxide-based thin film structures* (Elsevier, 2018), pp. 109–132.

[44]C. Kittel, *Introduction to Solid State Physics*, 8th (John Wiley and Sons, Inc, 2005) Chap. 2, pp. 23–43.

[45]J. Jo, Y. Tchoe, G.-C. Yi and M. Kim, 'Real-Time Characterization Using in situ RHEED Transmission Mode and TEM for Investigation of the Growth Behaviour of Nanomaterials', Scientific Reports **8**, 1694 (2018).

[46]A. Ichimiya and P. I. Cohen, *Reflection High-Energy Electron Diffraction* (Cambridge University Press, Dec. 2004).

[47]G. Rijnders and D. H. Blank, 'Real-Time Growth Monitoring by High-Pressure Rheed During Pulsed Laser Deposition', in *Thin films and heterostructures for oxide electronics* (Springer-Verlag, New York), pp. 355–384.

[48]S.-Q. Wu, S. Cheng, L. Lu, M. Liu, X.-W. Jin, S.-D. Cheng and S.-B. Mi, 'B-site ordering and strain-induced phase transition in double-perovskite La2NiMnO6 films', Scientific Reports **8**, 2516 (2018).

[49]J. P. Palakkal, T. Schneider and L. Alff, 'Oxygen defect engineered magnetism of La2NiMnO6 thin films', AIP Advances **12**, 035116 (2022).

[50]J. E. Kleibeuker, E.-M. Choi, E. D. Jones, T.-M. Yu, B. Sala, B. A. MacLaren, D. Kepaptsoglou, D. Hernandez-Maldonado, Q. M. Ramasse, L. Jones, J. Barthel, I. MacLaren and J. L. MacManus-Driscoll, 'Route to achieving perfect B-site ordering in double perovskite thin films', NPG Asia Materials **9**, e406–e406 (2017).

[51]P. Hofmann, 'Magnetism', in *Solid state physics*, 2nd ed. (Wiley-VCH, 2015) Chap. 8, pp. 171–181.

[52]B. Kim, J. Lee, B. H. Kim, H. C. Choi, K. Kim, J.-S. Kang and B. I. Min, 'Electronic structures and magnetic properties of a ferromagnetic insulator: La2MnNiO6', Journal of Applied Physics **105**, 07E515 (2009).

[53]M. Kitamura, I. Ohkubo, M. Kubota, Y. Matsumoto, H. Koinuma and M. Oshima, 'Ferromagnetic properties of epitaxial La2NiMnO6 thin films grown by pulsed laser deposition', Applied Physics Letters **94**, 132506 (2009).

[54]S. B. Kaemmer, 'Introduction to Brukers ScanAsyst and PeakForce Tapping AFM Technology', `https://blog.brukerafmprobes.com/wp-content/uploads/2015/08/AN133-Introduction_to_Brukers_ScanAsyst_and_PeakForce_Tapping_Atomic_Force_Microscopy_Technology_AFM_AN133.pdf`, *27/04/2022*.

[55]D. Neas and P. Klapetek, 'Gwyddion: an open-source software for SPM data analysis', Open Physics **10**, `10.2478/s11534-011-0096-2` (2012).

[56]'Statistical Analysis', `http://gwyddion.net/documentation/user-guide-en/statistical-analysis.html`, *30/04/2022*.

[57]I. J. A. Woollam Co., 'CompleteEASE Software Manual: Data Aquisition and Analysis Software for J.A. Woollam Co. Spectroscopic Ellipsometers', `https://wiki.nanotech.ucsb.edu/w/images/2/2e/CompleteEASE_Manual.pdf`, *17/06/2022*.

[58]M. Ohring, 'Characterization of Thin Films and Surfaces', in *Materials science of thin films* (Elsevier, 2002), pp. 559–640.

[59]J. A. Woollam Co., 'What is Ellipsometry?', https://www.jawoollam.com/resources/ellipsometry-tutorial/what-is-ellipsometry, *12/06/2022*.

[60]Yale Center for Environmental Law & Policy Center for International Earth Science Information and C. U. Network Earth Institute, 'Water and Sanitation Results', https://epi.yale.edu/epi-indicator-report/H2O, *12/06/2022*.

[61]R. Nabulsi and M. A. Al-Abbadi, 'Review of The Impact of Water Quality on Reliable Laboratory Testing and Correlation with Purification Techniques', Laboratory Medicine **45**, e159–e165 (2014).

[62]Z. Zhang and M. G. Lagally, 'Atomistic Processes in the Early Stages of Thin-Film Growth', Science **276**, 377–383 (1997).

[63]X. Song, D. Hong, Y. Wang, H. Liu, L. Liu and Y. Li, 'The Effect of Laser Energy and TargetSubstrate Distance on the Quality of CeO2 Seed Layer Deposited by PLD', Journal of Superconductivity and Novel Magnetism **24**, 1659–1663 (2011).

[64]S. Chakraverty, A. Ohtomo, M. Okude, K. Ueno and M. Kawasaki, 'Epitaxial Structure of (001)- and (111)-Oriented Perovskite Ferrate Films Grown by Pulsed-Laser Deposition', Crystal Growth & Design **10**, 1725–1729 (2010).

[65]A. Ojeda-G-P, C. W. Schneider, M. Döbeli, T. Lippert and A. Wokaun, 'Plasma plume dynamics, rebound, and recoating of the ablation target in pulsed laser deposition', Journal of Applied Physics **121**, 135306 (2017).

[66]F. Gunkel, L. Jin, D. N. Mueller, C. Hausner, D. S. Bick, C.-L. Jia, T. Schneller, I. Valov, R. Waser and R. Dittmann, 'Ordering and Phase Control in Epitaxial Double-Perovskite Catalysts for the Oxygen Evolution Reaction', ACS Catalysis **7**, 7029–7037 (2017).

[67]S. Chakraverty, A. Ohtomo, D. Okuyama, M. Saito, M. Okude, R. Kumai, T. Arima, Y. Tokura, S. Tsukimoto, Y. Ikuhara and M. Kawasaki, 'Ferrimagnetism and spontaneous ordering of transition metals in double perovskite La2CrFeO6 films', Physical Review B **84**, 064436 (2011).

[68]G. F. Harrington and J. Santiso, 'Back-to-Basics tutorial: X-ray diffraction of thin films', Journal of Electroceramics, 10.1007/s10832-021-00263-6 (2021).

[69]M. Yasaka, 'X-ray thin-film measurement techniques', The Rigaku Journal **26**, 1–9 (2010).

[70]I. Accu-Glass Products, 'Torr-Seal Low Vapor Pressure Resin Sealant Torr-Seal Mixing System Product Data Sheet', https://www.accuglassproducts.com/sites/default/files/download/outline/torr_seal_specifications.pdf, *14/06/2022*.

[71]Kurt J. Lesker Company, 'Torr Sealő Low Vapor Pressure Epoxy', https://www.lesker.com/newweb/fluids/sealants-epoxy/torrseal/, *14/06/2022*.

[72]F. Tang, T. Parker, G.-C. Wang and T.-M. Lu, 'Surface texture evolution of polycrystalline and nanostructured films: RHEED surface pole figure analysis', Journal of Physics D: Applied Physics **40**, R427–R439 (2007).

[73]I. Hallsteinsen, J. E. Boschker, M. Nord, S. Lee, M. Rzchowski, P. E. Vullum, J. K. Grepstad, R. Holmestad, C. B. Eom and T. Tybell, 'Surface stability of epitaxial La0.7Sr0.3MnO3 thin films on (111)-oriented SrTiO3', Journal of Applied Physics **113**, 183512 (2013).

[74]N. I. Kato, 'Reducing focused ion beam damage to transmission electron microscopy samples', Journal of Electron Microscopy **53**, 451–458 (2004).

[75]F. A. Stevie, C. B. Vartuli, L. A. Giannuzzi, T. L. Shofner, S. R. Brown, B. Rossie, F. Hillion, R. H. Mills, M. Antonell, R. B. Irwin and B. M. Purcell, 'Application of focused ion beam lift-out specimen preparation to TEM, SEM, STEM, AES and SIMS analysis', Surface and Interface Analysis **31**, 345–351 (2001).

[76]G. De Luca, J. Spring, U. Bashir, M. Campanini, R. Totani, C. Dominguez, A. Zakharova, M. Döbeli, T. Greber, M. D. Rossell, C. Piamonteze and M. Gibert, 'Ferromagnetic insulating epitaxially strained La2NiMnO6 thin films grown by sputter deposition', APL Materials **9**, 081111 (2021).

[77]R. G. Mitchell, 'Perovskites: Modern and Ancient', in *Perovskites: modern and ancient* (Almaz Press, Canada, 2003) Chap. 1-4.

[78]N. V. Krainyukova, V. O. Hamalii, A. V. Peschanskii, A. I. Popov and E. A. Kotomin, 'Low temperature structural transformations on the (001) surface of SrTiO3 single crystals', Low Temperature Physics **46**, 740–750 (2020).

[79]L. Gasparov, T. Jegorel, L. Loetgering, S. Middey and J. Chakhalian, 'Thin film substrates from the Raman spectroscopy point of view', Journal of Raman Spectroscopy **45**, 465–469 (2014).

[80]J. M. D. Coey, M. Venkatesan and P. Stamenov, 'Surface magnetism of strontium titanate', Journal of Physics: Condensed Matter **28**, 485001 (2016).

[81]M. S. Sheikh, A. P. Sakhya, A. Dutta and T. Sinha, 'Light induced charge transport in La2NiMnO6 based Schottky diode', Journal of Alloys and Compounds **727**, 238–245 (2017).

[82]T. N. Nunley, T. I. Willett-Gies, J. A. Cooke, F. S. Manciu, P. Marsik, C. Bernhard and S. Zollner, 'Optical constants, band gap, and infrared-active phonons of (LaAlO3) 0.3(Sr2AlTaO6)0.35(LSAT) from spectroscopic ellipsometry', Journal of Vacuum Science & Technology A: Vacuum, Surfaces, and Films **34**, 051507 (2016).

[83]M. L. Waalekalv, *Spectroscopic Ellipsometry of MoO3-x*, tech. rep. (Norwegian Universtiy of Science and Technology, Trondheim, 2016).

Appendix A

Parameters during pulsed laser deposition

The table is found on the following page.

Table A.1: Overview of the deposition parameters for growth of each thin film. T_{set} is the setpoint temperature as controlled in the instrument, while T_{thermo} is the temperature measured by the internal thermocouple close to the substrate holder. The pressure during depositions given by $P(O_2)_{dep}$, while the annealing pressure is given by $P(O_2)_{ann}$. The annealing time is given by t_{ann}, z_{target} gives the target z-position, $z_{substrate}$ the substrate z-position, E_{set} the energy setpoint for the laser, and $E_{measured}$ the measured laser energy in the viewport.

Sample	Substrate	Glue	T_{set} [C]	T_{thermo} [C]	$P(O_2)_{dep}$ [mbar]	$P(O_2)_{ann}$ [mbar]	t_{ann} [hours]	z_{target} [mm]	$z_{substrate}$ [mm]	Distance [mm]	E_{set} [mJ]	$E_{measured}$ [mJ]	Pulses No.
D-35/T-500	STO(111)	Epoxy	500		0.131	62.0	1	82	38	35	300	50	500
D-40	STO(111)	Epoxy	500	741.7	0.122	55.5	1.5	79	36	40	300	47.3	500
D-43	STO(111)	Epoxy	500	714	0.10	99.0	1	75	37	43	300	48	500
D-46	STO(111)	Epoxy	500	728	0.126	69.0	1	70	39	46	300	48	500
T-1500	STO:Nb(111)	Epoxy	500	730	0.123		1	75	36	44	275	45	1500
T-2000	STO(111)	Epoxy	500	714.6	0.103	66.0	1	82	37	36	300	47.2	2000
T-4000	STO(111)	Silver	500	679.1	0.0988	79.0	1	79	37	39	300	44.3	4000
X-1	STO(111)	Silver	500	707.4	0.114	56.0	1	76	37	42	300	45.4	1500

Appendix B

Additional XRD measurements

Here are results from additional XRD measurements on sample T-2000, where substrate and film peaks were hard to distinguish.

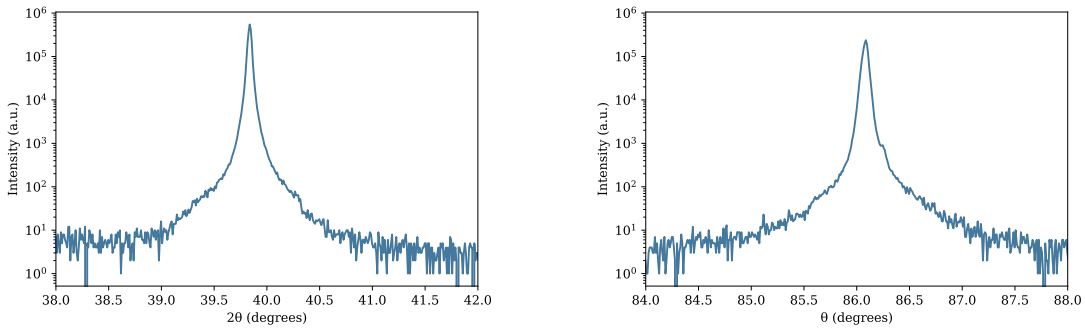

(a) (b)

Figure B.1: Magnification of the (a) (111) and (b) (222) peaks from the $\theta - 2\theta$ scan in Figure 4.13 show that the peaks are asymmetric and consists of contribution from substrate and film.

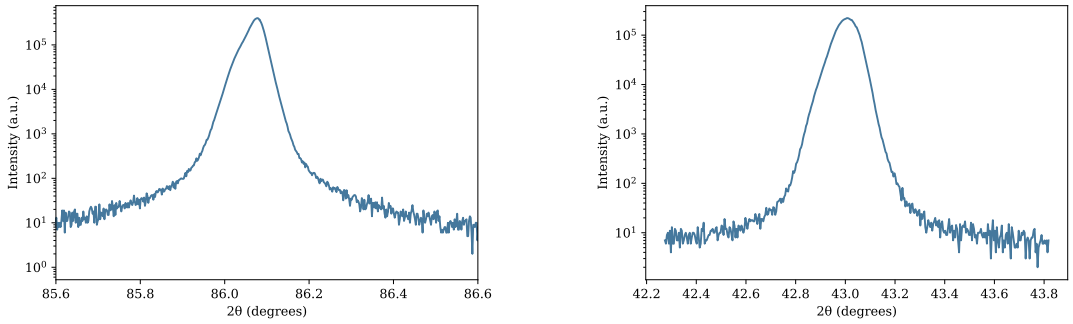

(a) (b)

Figure B.2: (a) Detector scan around the (222) diffraction peak, aligned to film. (b) $\theta - 2\theta$ scan around the (033) diffraction peak. Both scans show asymmetric diffraction peaks, but it is not possible to distinguish film from substrate.

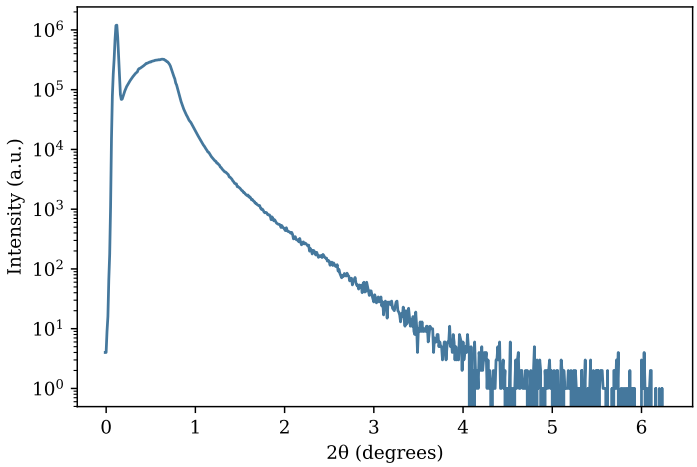

Figure B.3: X-ray reflectivity (XRR) scan. The scan does not display thickness fringes, that are necessary to determine film thickness from reflectivity scans.

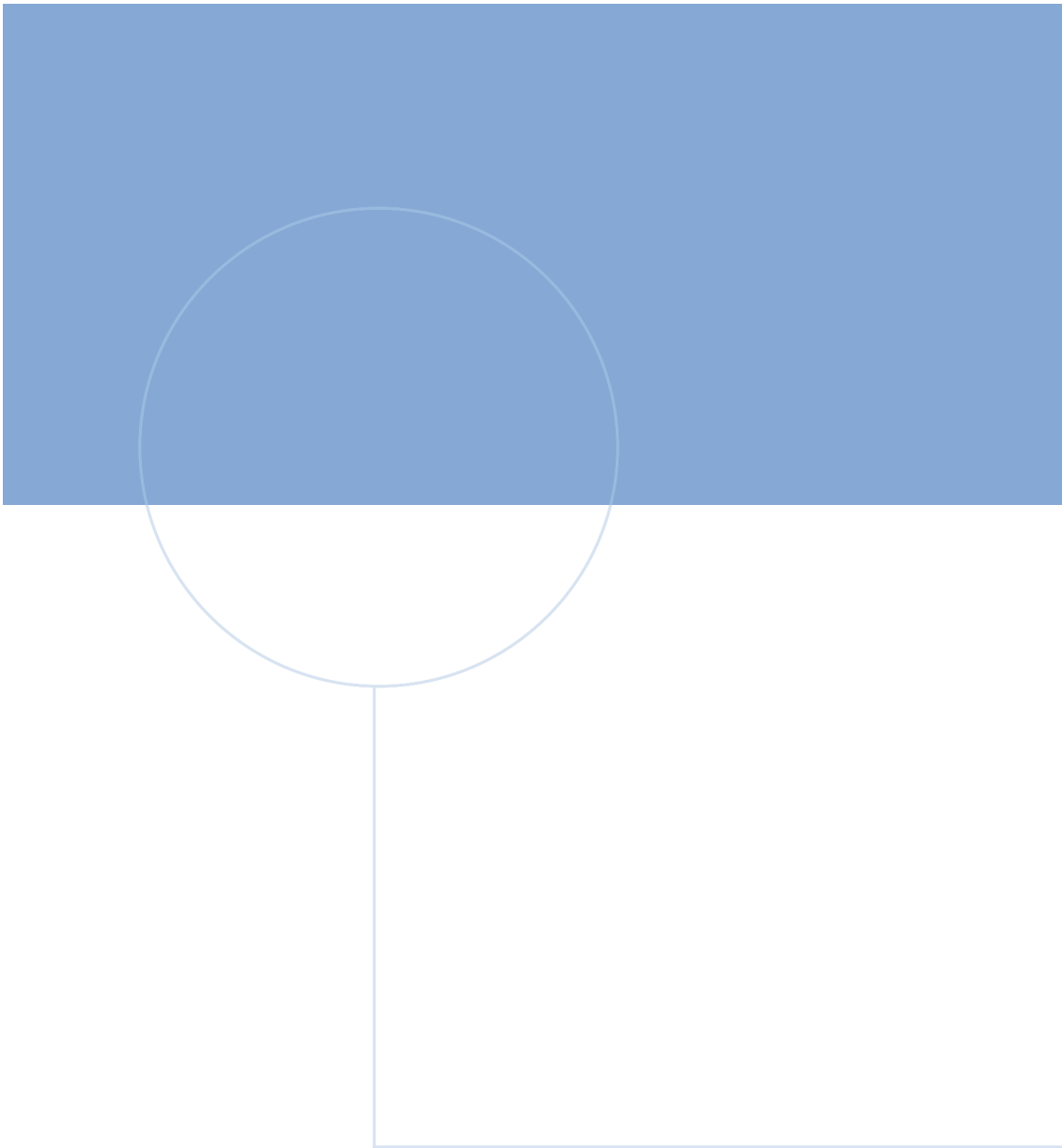

NTNU

Norwegian University of
Science and Technology